PHASE STABILITY AND THERMODYNAMIC ASSESSMENT OF THE NP-ZR SYSTEM

A Thesis

by

SAURABH BAJAJ

Submitted to the Office of Graduate Studies of
Texas A&M University
in partial fulfillment of the requirements for the degree of

MASTER OF SCIENCE

December 2010

Major Subject: Mechanical Engineering

PHASE STABILITY AND THERMODYNAMIC ASSESSMENT OF THE NP-ZR SYSTEM

A Thesis

by

SAURABH BAJAJ

Submitted to the Office of Graduate Studies of
Texas A&M University
in partial fulfillment of the requirements for the degree of

MASTER OF SCIENCE

Approved by:

Co-Chairs of Committee,	Raymundo Arróyave
	Tahir Cagin
Committee Members,	Patrice Turchi
	Sean M. McDeavitt
Head of Department,	Dennis O'Neal

December 2010

Major Subject: Mechanical Engineering

ABSTRACT

Phase Stability and Thermodynamic Assessment

of the Np-Zr system. (December 2010)

Saurabh Bajaj, B.Tech., Vellore Institute of Technology

Co-Chairs of Advisory Committee: Dr. Raymundo Arróyave
Dr. Tahir Cagin

Metallic fuels have an important role to play in "fast breeder" Gen-IV type nuclear reactors, and U-Pu-Zr is one of the prototypical systems. Because of the variability in fuel chemistry during burn-up, it is important to understand the effect of minor actinides and fission products on phase stability. Within this framework, we present a study on phase equilibria in the binary Np-Zr alloy system on which little work has been published. To resolve the contradictory reports on the ordering/clustering trends of the bcc phase, a thermodynamic study is performed using the CALPHAD method.

The calculated Np-Zr phase diagram is consistent with two sets of data: formation enthalpies of the bcc phase that are calculated with *ab initio* KKR-ASA-CPA electronic-structure method and lattice stabilities of solution phases obtained from first-principles technique. Another important feature in the Np-Zr alloy system is the non-stoichiometric δ-$NpZr_2$ phase that forms in a hexagonal C32 structure similar to the δ-phase in the U-Zr system and the ω-phase in pure Zr. An increase in the homogeneity range of the δ-phase when going from Pu to Np and to U is attributed to a lowering of its heat of formation that is caused by an increase in d-band occupation. Two different possibilities for the stability of the δ- and ω- phases have been proposed in the present work. Additionally, calculated changes in enthalpy versus temperature

are plotted for two alloy compositions of the Np-Zr system to guide future experimental work in resolving important issues in this system.

Finally, an *ab initio* study, implemented with the L(S)DA+U formalism, is performed for pure Np that reveals a transition from a non-magnetic to a magnetic state at a critical U parameter.

To Mom, Dad, and Sameer

ACKNOWLEDGMENTS

This work was supported by Lawrence Livermore National Laboratory under Task Order B575366 and Master Task Agreement B575363. The work of Alex Landa, Per Söderlind and Patrice Turchi has been done under the auspices of the US DOE by the Lawrence Livermore National Laboratory under contract No. DE-AC52-07NA27344. The TAMU-CONACYT program is acknowledged for partial support of A. Garay. The author would like to thank Tahir Cagin and Cem Sevik from the Department of Chemical Engineering, Texas A&M University for helpful discussions on this work. The help of Min Soo Park in the preparation of this thesis is acknowledged. First-principles calculations were performed with the Hydra supercomputer and the Chemical Engineering Cluster at Texas A&M University.

TABLE OF CONTENTS

CHAPTER Page

LIST OF TABLES

LIST OF FIGURES

FIGURE Page

FIGURE Page

CHAPTER I

INTRODUCTION

An ever-increasing demand on fossil fuels not only makes a country's economy energy dependent, but more importantly, affects the environment by releasing harmful exhaust gases into the atmosphere. It is also now well-realized that the future energy portfolio would not be dominated by any single alternate technology, but would be a mixture of contributions from various different sources, such as wind, solar, fuel cells, etc. A very promising source of energy that is sure to play an important role is nuclear energy. It has the capability of producing vast amounts of energy, and its most beneficial point is that it produces greenhouse-gas-free energy. Currently, nuclear energy provides 15% of the total global energy needs [1]. A major hindrance to increasing this number is waste disposal, which now stands at 12,000 tons per year worldwide [1]. This exorbitant amount of waste is radioactive in nature and thus needs to be carefully handled and deposited at safe sites. Also, due to the presence of weapon-grade plutonium in the waste, concerns are raised about the placement of such material in the hands of organizations that intend to misuse it, leading to nuclear proliferation.

A potential solution to this problem lies in the use of Generation-IV metallic fuel fast-breeder reactors. Metallic fuels have been a more popular choice for fuel materials for such reactors over oxides as they possess the capability of increasing power output by 30%, thus reducing operational costs and strengthening the economics of nuclear energy. In particular, the ternary uranium-plutonium-zirconium alloys have distinct

---

The journal model is *IEEE Transactions on Automatic Control*.

advantages in terms of reliability, reactor safety, and fuel cycle economics [2]. These materials, when used in fast breeder reactors, can transmute to minor actinides, such as Np, Am, and Cm, and other long-lived fission products due to the high burn-up rates at which these reactors operate [3]. The minor actinides and other products are further fissioned/recycled to produce more energy and reduce the amount of waste output, thus, closing the fuel cycle.

One of the issues with the use of metallic fuels is that the melting points of the actinides are significantly low: T_m[U] = 1135^0C, T_m[Np] = 639^0C, and T_m[Pu] = 640^0C [4, 5]. At high temperatures, there could be a problem of penetration of these actinides in the cladding. Thus, it becomes necessary to add high melting elements, such as Ti, Cr, Zr, Mo, to the fuels in order to increase their melting points to a safe limit. In particular, Zr metal is a good choice for alloying as: it possesses an additional capability of suppressing inter-diffusion between fuel and cladding, it has a very low thermal neutron cross-section thus making its alloys inherently safe, and it can be manufactured using standard fabrication techniques. All these benefits lead to the achievement of thermal and mechanical stability needed during operation of such reactors.

The present work is based on the thermodynamic study of the Np-Zr alloy system, which is a part of the series of alloys in discussion, and will aid in identifying/predicting phase behavior trends in similarly complex alloy systems. The information available in the literature on the Np-Zr system is scarce and at times, contradictory. Based on its position between uranium and plutonium in the actinide row of the periodic table, the alloy behavior of the Np-Zr system was expected [6–9] to be similar to the U-Zr and Pu-Zr systems. Broadly speaking, there were two

major noticeable trends from the phase diagrams of these systems: complete mutual solubility of the high-temperature (HT) body centered cubic (b.c.c) phases and, an elevation of melting points of the actinide alloys, relative to the pure phases. However, the results of several differential thermal analysis (DTA) and X-ray diffraction (XRD) experiments [6–10] pointed towards the immiscibility between the HT b.c.c phases, γ-Np and β-Zr. Thus, only small changes in the melting points and transition temperatures of Np-Zr alloys were found due to the resistance to mixing between Np and Zr. On the contrary, dilatometry, electron probe micro analysis (EPMA) and micrographic studies [11] showed the Np-Zr phase diagram to be completely ideal, i.e. complete solubility between the b.c.c phases γ-Np and β-Zr. These experimental works are discussed in detail in Chapter II.

Another key phase in the Np-Zr system that is important from the point of view of understanding phase formation behavior is the δ-$NpZr_2$ phase, analogous to the δ-UZr_2 phase in the U-Zr system [12–15]. This phase crystallizes in a C32 structure (space group:P6/mmm) similar to the ω-phase in pure Zr. The δ-$NpZr_2$ phase is known to stabilize due to an electron transfer from the actinide valence shell to the d-band transition element [12, 16]. Detailed discussions on this phase are also offered in Chapter II.

Even though there is a renewed interest in Zr-based actinide alloys, not much work has been done to study phase equilibria in these systems. Thus, to improve our understanding of phase stability, phase equilibrium, and thermodynamics for this system, it becomes necessary to develop a thermodynamic model based on the CALPHAD approach [17]. Chapter III presents the methodology and approach involved with this technique which involves the modeling of Gibbs energies of all the phases

taking part in equilibrium through reliable and consistent experimental data. Such a model offers many advantages, among them are: (1) it can be extrapolated to regions of temperatures and compositions which are not easily accessible by experiments, (2) and it provides an easy way to study how equilibria and reactions are affected by various external factors. The use of such techniques plays an even important role since experiments are challenging and expensive for this class of systems.

Ab initio calculations could also prove to be very helpful in determining ground-state properties of various phases present in this system. There is very little first-principles information available in the literature on the pure phases in this system. It is also worth noting that there is a lack in capability of current techniques available in handling highly correlated and localized systems such as the Np-Zr system we are dealing with in the current work. Chapter IV provides a brief introduction to the theory and concepts of the methods employed, and Chapter V presents the results of calculations performed using these methods.

A summary of the present work is provided in Chapter VI. Finally, in Chapter VII, it is explained how the results of this work fit within the larger context of determining phase equilibria in multi-component metallic fuel alloys, and directions on future work that will be undertaken to achieve this objective will be briefly discussed.

CHAPTER II

LITERATURE REVIEW

In this chapter, previous experimental and theoretical works are described in detail along with the results that have been obtained. Analysis and discussions on the conclusions made from these studies are also presented here.

A. Phase diagram

One of the first attempts to predict the Np-Zr phase diagram was made by John K. Gibson and Richard G. Haire [6]. The technique of differential thermal analysis (DTA) was employed as it is well-suited to study small sample elements and compounds. The DTA instrument used, was inserted into an inert-atmosphere glove box to prevent reaction with air and moisture. High-temperature (HT) studies were performed to study phase relationships, and determine the nature of the reactivity in the Np-Zr binary alloy system. Alloy samples were prepared by an *in situ* method, and since the melting temperature of Zr (1852^{o}C) was higher than the maximum limit of the DTA (1700^{o}C), the alloys were deemed equilibrated when consistent DTA thermograms were obtained. To measure transition enthalpies, the instrument was operated in the differential scanning calorimeter (DSC) mode to obtain heating and cooling curves and which were integrated. For pure Np, the transition temperatures and enthalpies were: 282^{o}C and 6.6 kJ mol^{-1} (α-orthorhombic $\rightarrow$ β-tetragonal), 578^{o}C and 3.9 kJ mol^{-1} (β-tetragonal $\rightarrow$ γ-bcc), 640^{o}C and 4.2 kJ mol^{-1} (γ-bcc $\rightarrow$ liquid). For pure Zr, the measured temperature and enthalpy of the α-hcp to β-bcc phase transformation were 840^{o}C and 3 kJ mol^{-1}. In the case of alloys, the primary focus was on determining if there was an elevation of melting point, when small amounts of Zr were added to Np, just as is the case in U-Zr and Pu-Zr alloys. For the 22,

48, and 50 at.% Zr samples, the DTA peaks largely resembled and corresponded to those obtained for the phase transformations in pure Np, thus suggesting that the bcc phases of Np and Zr are not completely miscible. This indicates that the Np-Zr phase diagram may be non-ideal and thus significantly different in character from the U-Zr and Pu-Zr systems.

More extensive DTA studies were performed [7], this time using both *in situ*, as previously employed, and *ex situ* (arc-melting) alloying methods. In addition to using a sample cup that was made of tantalum, Al_2O_3 cups were also used as it was found to be more resistant to a reaction with the molten alloys. Although the samples were heated up to 1400^oC, no clearly defined peaks were observed above 640^oC for any of them. Thermograms obtained for the 22 and 27 at.% Zr samples were very similar, and corresponded to the phase transitions in pure Np, implying that Zr was largely insoluble in Np. The middle transition at $\sim 550^oC$ in the 22 at.% Zr sample, manifested as an unresolved doublet indicating two closely spaced transitions. Later on, it will be seen from the phase diagram, that these transitions are attributed to the transitions from a two-phase equilibrium: β-Np + δ-$NpZr_2$ to another one: γ-Np + δ-$NpZr_2$, and then to: γ-Np + β-Zr.

Room-temperature (RT) X-ray diffraction (XRD) studies were performed on Np-Zr alloys with 10, 25, 50, 67, 75, and 90 at.% Zr [10]. The presence of four phases: α-Np, α-Zr, $NpZr_2$, and a phase corresponding to a stoichiometry of either Np_4Zr or Np_6Zr, was confirmed in all of the samples. The variation in cell volume of α-Zr, upon subsequent addition of Np, was obtained from X-ray data recorded after annealing of the 67 at.% Zr alloy. It was observed that as the annealing temperature was increased from 300-900^oC, there was a decrease in the cell volume of α-Zr, suggesting a decrease

in solubility of Np in α-Zr. On the contrary, the cell volume of α-Np remained unaffected upon addition of α-Zr, indicating negligible solubility of Zr in α-Np. Another conclusion made after studying the lattice parameters of α-Zr upon addition of Np, was that the a_0 parameter remained constant whereas, the c_0 parameter varied.

Based on the DTA and XRD results, a phase diagram of the Np-Zr system was proposed [8], shown in Fig. 1, consistent with all the experimental findings. Several of its features were deemed speculative. However, a miscibility gap between the HT bcc phases of Np (γ-Np) and Zr (β-Zr) was the essential information to be noted from the phase diagram.

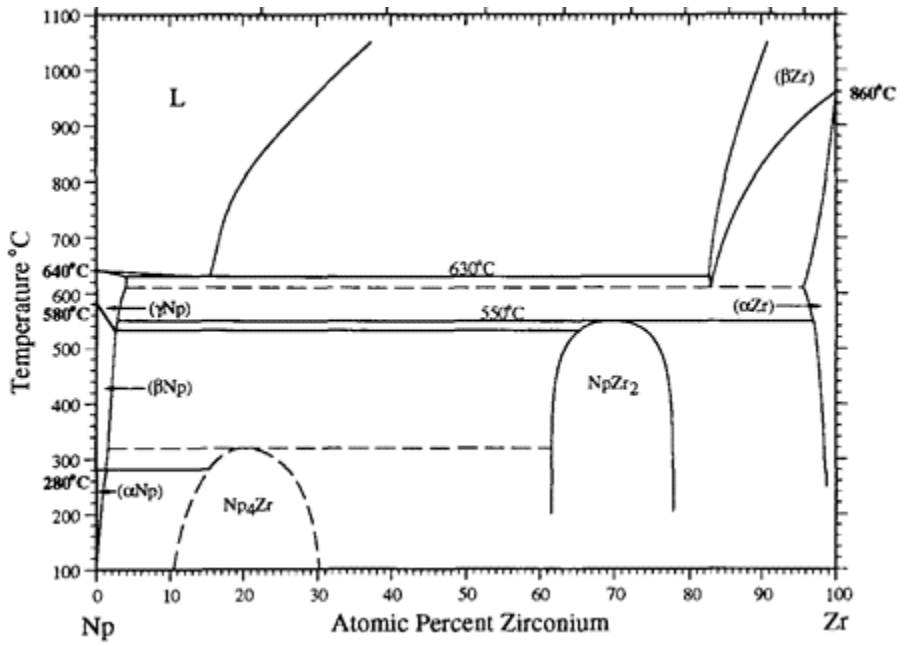

Fig. 1. Postulated Np-Zr phase diagram by Gibson *et al.* [8] based on XRD and DTA experiments.

With the aim of investigating the U-Zr-Np ternary system for determining the

properties of metallic fuels, Rodríguez *et al.* [11] performed dilatometry, electron probe microanalysis, and used micrographic techniques to determine the phases present, phase transformation temperatures, and melting points in the Np-Zr binary system. Three alloys of compositions 40, 72, and 91 at.% Zr were prepared by arc melting. Phase transformations of the alloys were determined by dilatometry using rods. Melting points were determined using a vertical dilatometer, and structures of the phases present were determined by annealing the alloys to high temperatures and then quenching them to several temperatures after which they were subjected to electron-probe microanalysis (EPMA) and microscopic examination. In accordance with results obtained from the experiments, a tentative phase diagram was drawn, as shown in Fig. 2, which was characterized by complete mutual solubility between γ-Np and β-Zr up to the melting point, which is in disagreement with previous findings [6–8, 10].

Ogawa *et al.* [16] performed a thermodynamic analysis on the Np-Zr system to determine the Gibbs excess free energies of mixing and free energies of transformations. The resulting phase diagram did agree qualitatively but not quantitatively with the one proposed in Ref. [8]. It was also mentioned that even though the interactions of Np and U with Zr do not significantly differ, the bcc miscibility gap intersects with the solidus resulting in limited mutual solubility (see Fig. 1).

To answer important questions about the topology of the phase diagram, Okamoto *et al.* [9] investigated by XRD analysis two alloys at compositions 67 and 75 at.% Zr between 25 and 700^{o}C. Phases observed in both samples at different temperatures were similar. At room temperature, diffraction lines obtained were due to α-Np, δ-$NpZr_2$ or α-Zr. The bcc phase of Zr was not observed even up to 700^{o}C suggesting

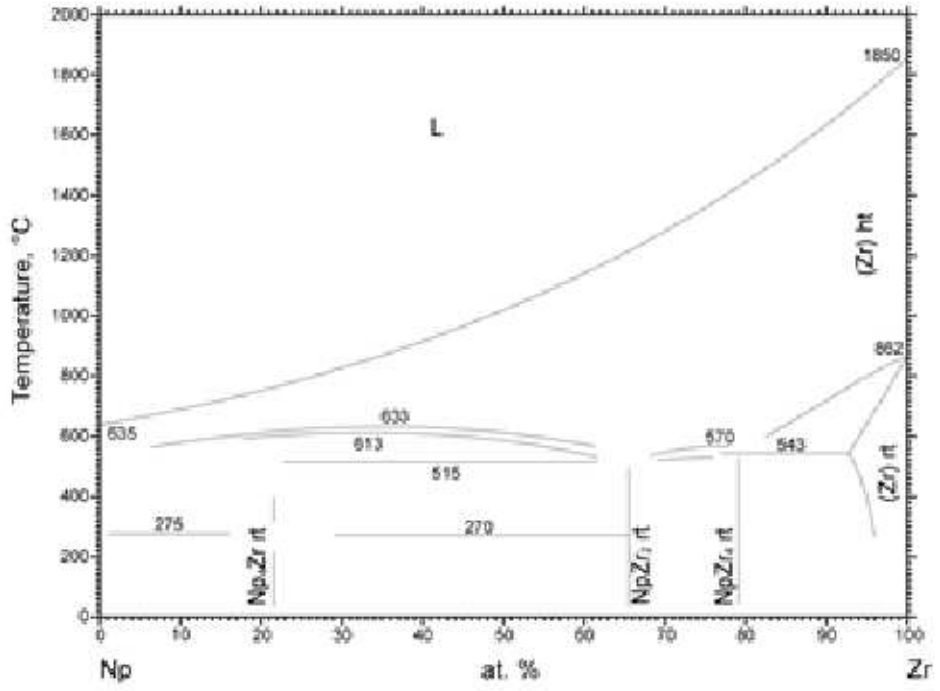

Fig. 2. Postulated Np-Zr phase diagram by Rodríguez *et al.* [11] based on the results of dilatometry and EPMA.

low solubility of Np in β-Zr. From the differences in atomic radii and lattice parameters of γ-Np and β-Zr, the solubility of Zr in γ-Np was found to be ~ 4 at.%. These results are in accordance with the tentative phase diagram shown in Fig. 1.

B. δ-$NpZr_2$

The DTA thermograms obtained by Gibson and Haire [6] for the two samples at ~ 50 and 75 at.% Zr, showed no peaks at low temperatures due to the $\alpha \rightarrow \beta$ transition in neptunium, suggesting that some Zr was dissolved. In addition, the single peak that appeared at $\sim 540^{o}$C for the 75 at.% Zr sample, may be assigned to an intermediate

Zr-rich phase. Both observations point to the presence of a δ-$NpZr_2$ phase, similar in stoichiometry to the δ-UZr_2 phase found in the U-Zr system [12–14, 18]. These results were confirmed in a study where different methods of alloying (*in situ* and *ex situ*) and cup materials (Ta and Al_2O_3) were used [7]. Also, since all the DTA results suggested that the analog of the bcc solid solution in U-Zr does not exist in the Np-Zr system, it was believed that formation of the δ-phase occurred from Np-rich and Zr-rich solid phases, which, as will be seen later, could be assigned to γ-Np and α-Zr, respectively.

The 50 and 75 at.% Zr samples, prepared by arc-melting, were also subjected to RT powder XRD [7]. It was found that both samples were dominated by the same phase whose diffraction lines were assigned to bcc phase. However, in Ref. [13], it was shown that the δ-phase is comprised of four hexagonal cells that were oriented in such a way that the X-ray lines would point to a cubic symmetry. Thus, the actual symmetry of the δ-phase is hexagonal, and not bcc.

It has been concluded from previously reported XRD and neutron diffraction results on the δ-UZr_2 phase [13–15], that the diffraction pattern obtained agree best with a partially ordered and modified C32 structure, similar to the ω-phase of Zr as shown in Fig. 3, in which a Zr atom occupies the (0, 0, 0) position, and U and Zr atoms are randomly located at the $(\frac{2}{3}, \frac{1}{3}, \frac{1}{2})$ and $(\frac{1}{3}, \frac{2}{3}, \frac{1}{2})$ sites. In the study performed by Gensini *et al.* [8], the XRD lines coincided with a structure for the δ-$NpZr_2$ phase, thus confirming the assumption. The only experimentally validated data on the composition range of the δ-phase was mentioned in the work by Rodríguez *et al.* [11], where it was found that this phase extends from about 65.3 to 78.2 at.% Zr.

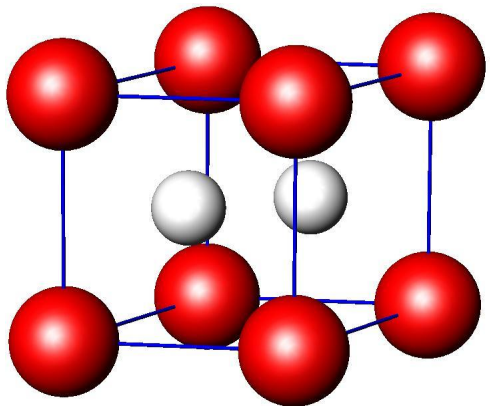

Fig. 3. The hexagonal ω-C32 structure.

Further reasoning for the appearance of diffraction lines that corresponded to a bcc structure instead of the hexagonal ω-structure was provided by Ogawa *et al.* [16]. It was shown that if in a bcc structure, two of the three equidistant (111) planes move towards one another along the [111] direction, and collapse into one while the third remains in its original position, the resulting structure is the so-called ω or C32 structure.

The temperature and extent of formation of the δ-phase, which are important features in the Np-Zr phase diagram, were analyzed with XRD experiments performed by Okamoto *et al.* [9]. The intensity of the diffraction lines corresponding to $NpZr_2$ was found to be much stronger in the 75 at.% Zr alloy than at 67 at.% Zr which, in principle, is the stoichiometric composition for this solid solution, thus indicating a wide composition range of stability for this phase. The temperature of formation was found to be $\sim 550^{o}$C, and since, at this temperature, γ-Np and α-Zr are the stable forms, it was concluded that $NpZr_2$ forms from γ-Np and α-Zr. As its formation is not from a single mutual solid solution, like in the U-Zr system, this results in slow

formation kinetics and a shift in stoichiometry for this phase.

C. ω-Zr

As described in the previous section, the δ-$NpZr_2$ phase is structurally similar to the ω-phase solid solution. The ω-phase has been the subject of numerous theoretical and experimental works that started more than fifty years ago when it was first discovered.

The ω-phase was first discovered by a high-pressure X-ray technique conducted by Jamieson [19] in Ti and Zr. At high pressures, the diffraction patterns and intensities corresponded to the ω-phase with a hexagonal symmetry and, as a distortion of the bcc phase. The lattice points were determined to be (0, 0, 0), ($\frac{2}{3}$, $\frac{1}{3}$, $\frac{1}{2}$) and ($\frac{1}{3}$, $\frac{2}{3}$, $\frac{1}{2}$).

It is well known that the hcp structure of Zr is the stable phase at ambient pressure and temperature and that it transforms to the bcc phase at higher temperatures. However, when pressure increases at ambient temperature, Zr first undergoes a $\alpha \rightarrow \omega$ transformation and then a $\omega \rightarrow \beta$ transformation as shown in Fig. 4. Botstein *et al.* [20] studied the $\alpha \rightarrow \omega$ phase transformation in Zr using high pressure techniques. It was concluded that at ambient pressure, and temperatures less than 200 K, the ω-phase is the stable phase of Zr. Enthalpy of transformation, $\Delta H_{Zr}^{\alpha \rightarrow \omega}$, was found to be -553 J/mole. This small value indicates the slow kinetics in ω-phase formation at low temperatures, and is in accordance with the result of having only small amounts of this phase present in the sample. This conclusion was confirmed by theoretical calculations performed by Vohra [21], from which the results indicated a possibility of retaining the ω-phase in a metastable form after pressure release at

ambient conditions. Impurities in samples also plays an important role and may affect the occurrence of this phase. A hysteresis effect was also observed with temperature during this transformation. This phenomenon of marginal stability or metastability of the ω-phase against the hcp phase became the subject of numerous *ab initio* works to determine the ground state of Zr. However, due to the extremely small difference in energy between these phases, the results pointed to two different conclusions: the ω-phase is the lowest energy phase of Zr [22–24] or, the hcp phase is the lowest energy phase of Zr [25–28]. This ambiguity seems to remain unresolved, and due to this uncertainty, both possible scenarios are considered in the present work. Model 1 will be calculated considering the hcp phase as the ground state of Zr and, Model 2 will be calculated considering the ω-phase as the ground state of Zr.

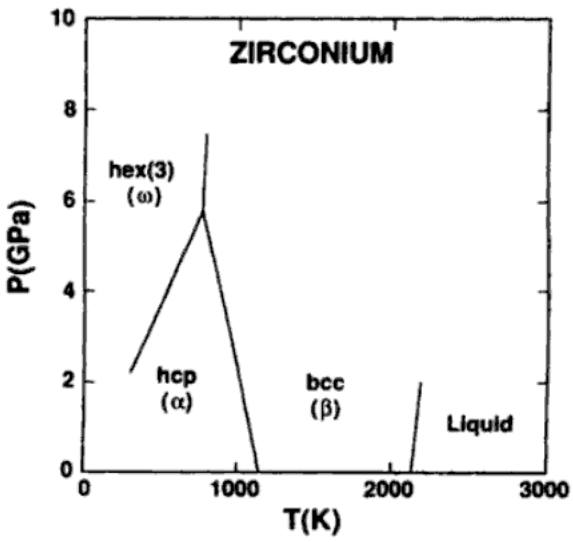

Fig. 4. The pressure-temperature phase diagram of Zr [29].

The role of d-electrons in stabilizing different phases in the transition metal series was investigated by Pettifor [30] from band energy calculations within the atomic

sphere approximation (ASA). It was found that atomic levels broadened into bands and changed their energies and occupation, particularly the d-band whose contribution was more important than for other bands. It was also pointed out that pressure changes also lead to a change in d-band occupancy, as shown in Fig. 5, triggering a phase change in these elements. Under compression, the s-band is pushed toward the core region, decreasing the s-d spacing, and thus increasing the d-band occupancy. This was confirmed in an electronic structure study by Vohra *et al.* [31] on the α and ω phases of Zr. The band structure results showed a decrease in s-d spacing at high pressures that was confirmed by an X-ray photoelectron spectroscopy (XPS) study.

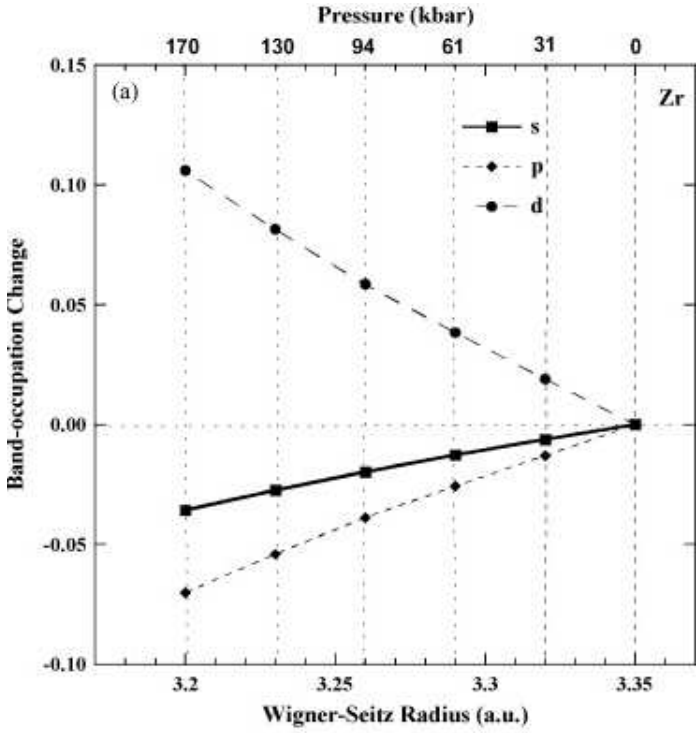

Fig. 5. Changes in *s*-, *p*-, and *d*-band occupations as functions of Wigner-Seitz radius calculated from FPLMTO calculations [12].

The d-electron role in stabilizing the ω-phase and its alloys was studied extensively by Vohra [32]. It was concluded that the ω-phase in pure transition metals and their alloys can be stabilized at high pressure and, be retained at ambient conditions in a metastable state after appropriate thermal and pressure treatments. The relative stability of different crystal structures was measured by the bonding contribution of the d-band, U_d^{bond}, given by,

$$U_d^{bond} = \int_{E_b^d}^{E_f} n_d(E)(E - C_d)dE \tag{2.1}$$

where, E_f is the Fermi energy, E_b^d is the bottom of the d-band, $n_d(E)$ is the density of states of the d-band, and C_d is the center of gravity of the d-band. Thus, the structure that has the lowest value of U_d^{bond} is the most energetically favorable for a given d-band occupancy, $n_d(E)$. This proposition was studied by calculating bonding energies of the α, ω, and β phases as a function of the change in d-band occupation at RT and pressure as shown in Fig. 6. The result showed that as d-electrons were added, the bonding energy of the α-phase was the lowest, followed by the ω-phase and lastly, the β-phase.

The theory according to which an increase in the number of d-electrons governs the structural phase stability in transition elements, was tested by high-pressure XRD experiments [33, 34]. The hcp $\rightarrow \omega \rightarrow$ bcc phase transitions were observed at pressures of 67 kbar and 330 kbar.

XRD analysis by Xia *et al.* [35] found the bcc phase of Zr to stabilize at high pressures, in accordance with the theory of stabilization of bcc structures of transition metals at high pressures due to an increase in the d-band occupancy. In a follow-up

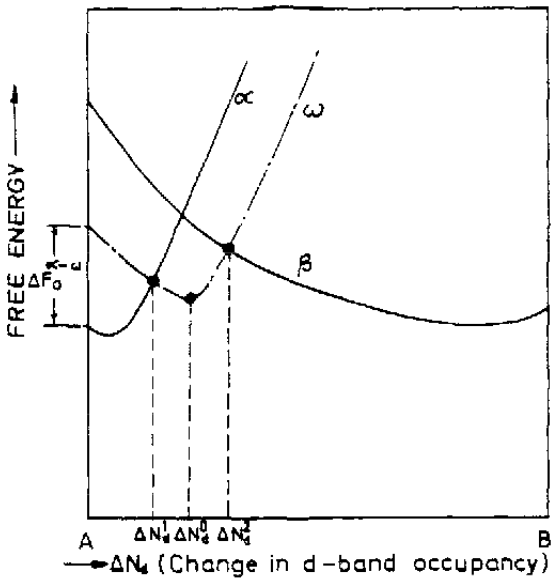

Fig. 6. Bonding energy of the α, ω, and β phases as a function of a change in d-band occupation for an AB alloy system [32].

work, Xia *et al.* [36] performed XRD experiments and assigned the equilibrium transformation pressure, at room temperature, to be 350 kbar between ω-Zr and bcc-Zr.

The model of the $\beta \rightarrow \omega$ transformation was first proposed by Hatt *et al.* [37] after correlating a model with results from XRD data. A gliding of $\{112\}_\beta$ planes along the $\langle 111 \rangle_\beta$ direction results in a sequence that corresponds to the formation of the hexagonal C32 structure. It was later adopted in several work as the bcc to ω transformation mechanism in Zr [16, 25, 38, 39].

In the case of alloys, if the alloying element can supply electrons to the d-band, a compound, having a structure similar to the ω-structure in Zr, can be stabilized at a certain composition in the system. Many works have been devoted to the study of this

alloying effect which is equivalent to pressure application [12, 32, 40–43]. This phase transition series was also noted from the plot of structural energy differences obtained from canonical bands, as a function of d-band occupancy [44]. With an increase in pressure, hcp initially transforms to C32, and then to bcc. On the experimental side, this was confirmed by high-pressure studies on alloys [45, 46] that indicated the stabilization of ω-phase type structures due to an increase in pressure at some alloy compositions. In an analysis of the stabilization of the δ-phase [16], it was concluded that the C32 structure is stabilized with respect to α-Zr (hcp) by the addition of Np, thus suggesting favorable mixing between the valence shells of the actinide and the d-shell of Zr.

D. θ-Np_4Zr

In Ref. [10], a phase, whose diffraction lines did not correspond to either Np, Zr or $NpZr_2$, was observed in all samples of compositions 10, 25, 50, 67, 75, and 90 at.% Zr. These lines were in better agreement with those corresponding to a compound of stoichiometry Np_4Zr, rather than Np_6Zr, and may have a counterpart in the Pu-Zr system [47, 48].

E. Phases of pure Np

Neptunium metal exhibits three allotropic forms, α-, β-, and γ-phases [49] as shown in Table I.

The decreasing trend toward magnetism as one goes from U, which is a superconductor, to Np and Pu which are non-superconducting but have a tendency toward magnetism, and then to Am, Cm, Bk which appear to have well-defined local moments [50, 51], has been attributed to an increase in f-d hybridization along the

Table I. Crystal structure data of pure Np [49].

Phase	Symmetry	Lattice parameters (Å)			Density (g/cm^3)
		a	b	c	
α	Orthorhombic (Pnma)	6.663	4.723	4.887	20.45
β	Tetragonal (P4/nmm)	4.897	4.897	3.388	19.36
γ	Bcc (Im3m)	3.526	3.526	3.526	18.00

actinide series of the periodic table [52]. Thus, actinide metals may be separated into two groups: first being from Th up to Pu, in which 5f electrons are in narrow bands hybridized with the 6d ones, while in the second group starting with Am, a more standard lanthanide behavior is observed, where the 5f states are localized below the Fermi energy. All of this adds up to Np being exchange-enhanced, nearly magnetic metal. However, as seen from the nuclear magnetic resonance (NMR) and Mössbauer effect (ME) measurements, it does not order magnetically [53].

The measured atomic volume of Np was found to be $\sim$ 12 cm^3/gram-atom [4], which happens to be the lowest in the actinide series. The similarity between the trends in atomic volume of the light actinides (Th-Np) and the transition metals suggested, early on, that the light actinides were part of a 6d transition series. There is then a sharp increase in volumes from Np to Am (with Pu being in the middle), after which the trend is similar to that of the lanthanides [4]. The cohesive energy and bulk modulus of Np is found to be $\sim$ 481 kJ/mol and $\sim$ 750 kbar, respectively [4]. The thermal conductivity of actinides falls with an increase in atomic number and reflects an increase in electrical resistivity. These facts point to the important role played by electrons. Thermal conductivity is mostly independent of temperature and for Np is found to be $\sim$ 7 Wm^{-1}K^{-1} [4]. The calculated maximum in f-electron contribution

to metallic bonding in Np coincides with the smallest metal-metal distance and the lowest melting point among the actinides. The average atomic distance is 3.0 Åin the α-phase, 3.03 Åin the β-phase, and 3.05 Åin the γ-phase [4]. Thus, high-temperatures do not affect the degree of f-f overlap, and this observation is consistent with the non-magnetic behavior of Np.

CHAPTER III

THE CALPHAD METHOD

The thermodynamics of solution phases is first described here as it forms the fundamental basis of the CALPHAD method. Solution is a term refered to a system in a solid, liquid or gaseous state, which exhibits solubility between the various components that make up the system. With relevance to the present work, thermodynamics of two-component systems or binary solutions will be dealt with in the following.

A. Ideal mixing

Ideal mixing represents an ideal case of no mixing or interactions in solutions. Statistical thermodynamics defines entropy in terms of disorder in the system. Kelvin and Boltzmann gave a mathematical formulation of this definition as:

$$S = k \, log_e W \tag{3.1}$$

where, k is Boltzmann's constant and W is a measure of disorder in the system. If in a binary solution, out of a total of N sites n sites are occupied by A-type of atoms and the rest, $(N - n)$ sites, by B-type atoms as shown in Fig. 7,

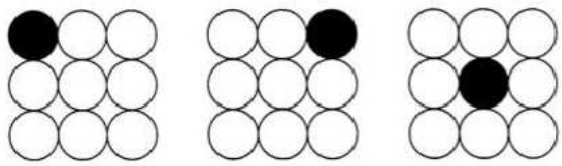

Fig. 7. Schematic representation of random mixing of A and B atoms/molecules in a binary solution [17].

The disorder or probability of distribution in this case is given by,

$$W = \frac{N!}{n!(N - n)!} \tag{3.2}$$

The entropy of this solution then is,

$$S = k\ log_e \frac{N!}{n!(N - n)!} \tag{3.3}$$

After applying Stirling's approximation and subsequent simplifications, the entropy change for ideal mixing is given by,

$$S = -R(x_a log_e x_a + x_b log_e x_b) \tag{3.4}$$

Thus, the Gibbs energy of mixing in case of no interactions between constitutive elements is given by,

$$G_{mix}^{ideal} = RT(x_a log_e x_a + x_b log_e x_b) \tag{3.5}$$

B. Non-ideal mixing

In reality, there is always some kind of interactions between different atom types in a solution. These interactions can either be attractive or repulsive in nature. The effects of such interactions are incorporated via the excess mixing energy term, G_{mix}^{xs}, which is modeled in the simplest way according to the regular solution model:

$$G_{mix}^{xs} = \Omega\ x_a x_b \tag{3.6}$$

where, Ω is a regular solution parameter. Its sign depends on the nature of chemical interactions, positive for repulsive and negative for attractive interactions. The tendency to form a miscibility gap or two-phase structures in binary solution phases

increases with an increase in magnitude of this regular solution parameter. In the case of attractive interactions or negative values of the regular solution parameter, the tendency is to form continuous solid solutions.

Equations (3.5) and (3.6) combine to give the Gibbs energy of solution,

$$G_{mix} \;=\; RT(x_a log_e x_b \;+\; x_b log_e x_b) \;+\; \Omega\; x_a x_b \tag{3.7}$$

However, in the presence of crystallographically distinct phases, the Gibbs energy at end-points of the mixing curve have to be calculated, thus requiring to define reference states for the pure components. The Gibbs energy is then written as,

$$G \;=\; G_{ref} \;+\; G^{ideal}_{mix} \;+\; G^{xs}_{mix} \tag{3.8}$$

where G_{ref} is given by,

$$G_{ref} \;=\; \sum_i x_i G^o_i \tag{3.9}$$

where, x_i is the mole fraction of component i, and G^o_i is the Gibbs energy of the phase for pure component i.

C. Thermodynamic models

Solution phases are modeled via various methods, two of which are described here.

1. Random substitutional model

In this model, the components occupy crystal sites in a random manner rather than in an ordered manner, as shown in Fig. 8. Thus, gases, liquids and some metallic solid solutions are represented very well by this model.

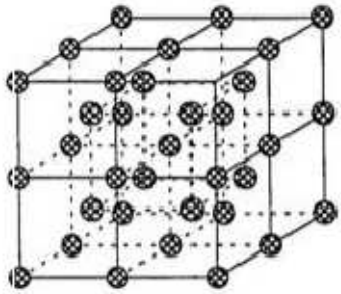

Fig. 8. Random occupation of sites on a bcc structure [17].

In the present work, the liquid, orthorhombic, and tetragonal phases are modeled in this manner. One of the simplest non-ideal models is the regular solution model which considers no dependence of the nature of interactions between the components on the composition of the solution. The Gibbs free energy expression of such a model is given similar to (3.8) as,

$$G_m^{\phi} \;=\; \sum_{i=Np,Zr} x_i \; {}^{o}G_i^{\phi} \;+\; RT \sum_{i=Np,Zr} x_i log_e x_i \;+\; x_{Np} x_{Zr} L_{Np,Zr}^{\phi} \tag{3.10}$$

where, G_m^{ϕ} denotes the Gibbs energy of phase ϕ, x_i is the mole fraction of component i, ${}^{o}G_i^{\phi}$ defines the Gibbs energy of the phase containing the pure component i, obtained from the SGTE database [54] and, $L_{Np,Zr}^{\phi}$ is an interaction parameter that incorporates the effects of non-ideal mixing. To account for dependencies on changes in composition, this parameter is expanded using Redlich-Kister formalism [55] as,

$$L_{Np,Zr}^{\phi} \;=\; \sum_{v} L_{Np,Zr}^{\phi} (x_{Np} \;-\; x_{Zr})^{v} \tag{3.11}$$

The above equation for G_{mix}^{xs} is considered a regular solution when $v = 0$ and non-regular solution when $v > 1$. Th binary interaction parameter is made temperature-

dependent using,

$$ {}^{v}L^{\phi}_{Np,Zr} \;=\; {}^{v}A \;+\; {}^{v}BT \tag{3.12} $$

where ${}^{v}A$ and ${}^{v}B$ are model parameters to be optimized.

2. Sublattice model

This method of modeling phases can be applied to a variety of phase types such as interstitial and solution phases. The sublattice model can be visualized as consisting of interlocking sublattices as shown in Fig. 9.

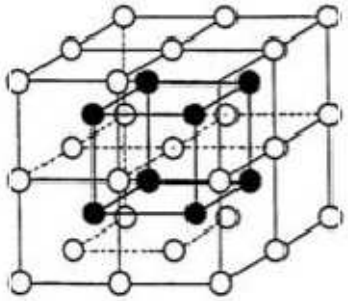

Fig. 9. A bcc structure shown with preferential occupation of sites by atoms on the two simple cubic sublattices [17].

Its crystalline nature does not particularly represent a crystal structure within its general definition, however, certain external terms and conditions can be imposed to simulate special structure types. In this method it is necessary to define the fractional site occupation of each component in all the sublattices, which is given by,

$$ {}^{s}y_i \;=\; \frac{n_i^s}{N^s} \tag{3.13} $$

where n_i^s is the number of atoms of component i on sublattice s.

In many cases when vacancies are involved and become important to model a phase, such as an intermetallic phase, the site occupation is modified as,

$$ {}^{s}y_i \;=\; \frac{n_i^s}{n_{Va}^s \;+\; \sum_i n_i^s} \tag{3.14} $$

where n_{Va}^s gives the number of vacancies on sublattice s.

The Gibbs energy reference state is obtained when only pure components can be considered as existing on each sublattice, and is given by,

$$ G_m^{ref} \;=\; \sum_{I0} P_{I0}(Y)^o G_{I0}^{\phi} \tag{3.15} $$

where P_{I0} represents the corresponding product of site fractions when each sublattice is occupied by only one component. In general, P_{IZ} is the site fraction product when only one sublattice contains Z components and the remaining sublattices are occupied by one component. G_{I0}^{ϕ} is the Gibbs energy of the compound defined by I in phase ϕ. For example, if a two-sublattice phase is modeled as $(A,B)_1(C,D)_2$, where A, B, C and D are the components of this phase, the Gibbs energy reference state is written as,

$$ G_m^{ref} \;=\; y_A y_C G_{AC}^o \;+\; y_A y_D G_{AD}^o \;+\; y_B y_C G_{BC}^o \;+\; y_B y_D G_{BD}^o \tag{3.16} $$

The ideal entropy of mixing in this case is given by,

$$ G_{mix}^{ideal} \;=\; RT \sum_s N^s \sum_i y_i^s log_e y_i^s \tag{3.17} $$

Vacancies are included in the fractional site occupation term, y_i^s. The ideal entropy

term in the above expression, includes all possible configuration contributions by all components mixing in each sublattice.

The Gibbs excess energy of mixing for the two-sublattice system described previously as $(A, B)_1(C, D)_2$, is given by,

$$G^{xs}_{mix} \;=\; y^1_A y^1_B L^0_{A,B:*} \;+\; y^1_C y^1_D L^0_{*:C,D} \tag{3.18}$$

The above equation represents the regular solution format, and $L^0_{A,B:*}$ and $L^0_{*:C,D}$ are the regular solution mixing parameters for each sublattice that are independent of the site occupation on the other sublattice. The sub-regular format includes the site occupation on the other sublattice as,

$$G^{xs}_{mix} \;=\; y^1_A y^1_B y^2_C L^0_{A,B:C} + y^1_A y^1_B y^2_D L^0_{A,B:D} + y^1_C y^1_D y^2_A L^0_{A:C,D} + y^1_C y^1_D y^2_B L^0_{B:C,D} \tag{3.19}$$

Similar to the formalism in the case of the random solution model, the parameters are made composition dependent as,

$$L^0_{A,B:C} \;=\; y^1_A y^1_B y^2_C \sum_v L^v_{A,B:C} (y^1_A \;-\; y^1_B)^v \tag{3.20}$$

The other parameters are modeled in a similar manner. The final Gibbs excess energy of mixing is given by,

$$G^{xs}_{mix} \;=\; \sum_{Z>0} \sum_{IZ} P_{IZ}(Y) L^{\phi}_{IZ} \tag{3.21}$$

Thus, the total Gibbs energy of this phase is obtained by combining the reference energy, ideal entropy contribution and excess energy contribution from (3.15), (3.17) and (3.21), respectively, which is given by,

$$G_m^{\phi} \;=\; \sum_{I0} P_{I0}(Y)^o G_{I0}^{\phi} \;+\; RT \sum_s N^s \sum_i {}^s y_i log_e {}^s y_i \;+\; \sum_{Z>0} \sum_{IZ} P_{IZ}(Y) L_{IZ}^{\phi} \quad (3.22)$$

D. Evaluation of Gibbs energy parameters

After having made a decision of the model for the Gibbs energy of each phase to be considered for a given system, and entering all experimentally measured quantities in an input file (.POP), the next step in the CALPHAD method is the evaluation of the parameters. This is carried out using an optimizer code that essentially revolves around Gibbs energy minimization. This type of code is based on the aim of reducing the statistical error between the experimental data and the calculated phase equilibria as much as possible.

1. Minimization procedure for single-phase equilibria

In the case of solution phases where enthalpies and entropies are temperature dependent, the Gibbs energy minimization is carried out by minimizing the function,

$$\Delta G^{1\phi} \;=\; \sum_i x_i^{\phi} \overline{G}_i^{\phi} \;-\; G^{\phi} \;=\; 0 \quad (3.23)$$

A Newton-Raphson method is used for rapid convergence. An initial temperature is chosen and both $\Delta G^{1\phi}$ and $\Delta G^{1\phi}/dT$ are calculated and then used to estimate a new temperature where $\Delta G^{1\phi}$ is expected to be equal to zero as shown in Fig. 10. If this new temperature does not satisfy the convergence condition, a new temperature is chosen. This process is repeated until $\Delta G^{1\phi}=0$.

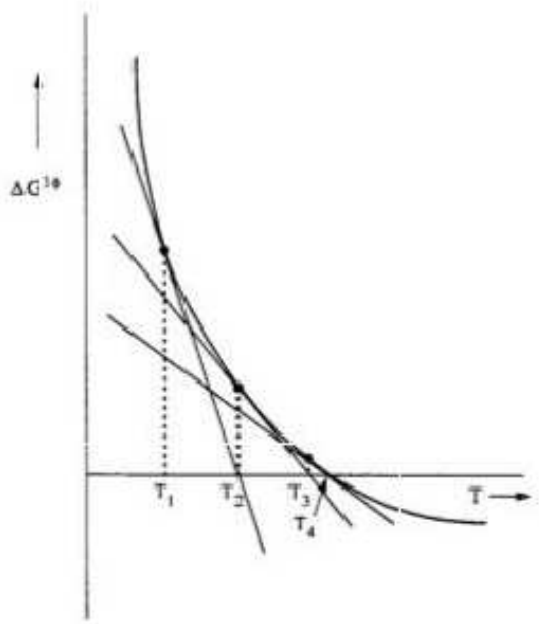

Fig. 10. Schematic diagram showing the process of calculating the temperature at which $\Delta G^{1\phi}=0$ [17].

2. Minimization procedure for two-phase equilibria

The following mass balance equations will be utilized in the calculation of a two-phase equilibria,

$$N_i \;=\; \sum_{\phi} N_i^{\phi} \tag{3.24}$$

and,

$$\sum_{i} N^i \;=\; M \tag{3.25}$$

where, N_i is the total number of mole of component i in the system, N_i^{ϕ} is the number of moles of component i in phase ϕ and, M is the total number of moles in the system.

The following is the presentation of the general minimization procedure. At first, the phase equilibrium is assumed to be single-phase. Then, an arbitrary amount of the second phase is introduced in the system and in accordance with the mass balance equations, a corresponding change is made in the composition of the first phase followed by the calculation of the Gibbs energy. The composition of this phase is then kept constant and the amount of the second phase is then varied with a corresponding change in its composition, to maintain mass balance, so that the Gibbs energy is minimized as shown in Fig. 11.

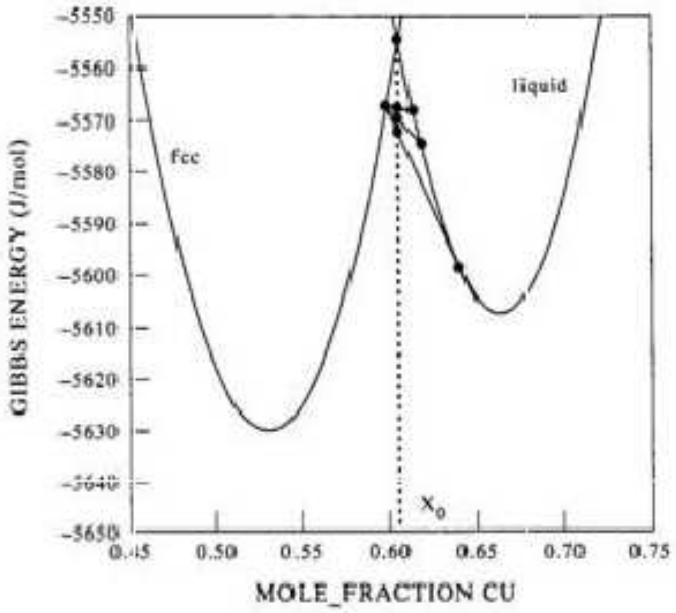

Fig. 11. First stage in the iteration process of Gibbs energy minimization of a Cu-Ni alloy at composition x_0 in Cu, and at 1523 K [17].

The selection of the amount of the second phase to be varied can be made by calculating the second derivative of G with respect to N^{liq} to obtain the composition at which $dG/dN^{liq}=0$, as shown in Figs. 12 and 13.

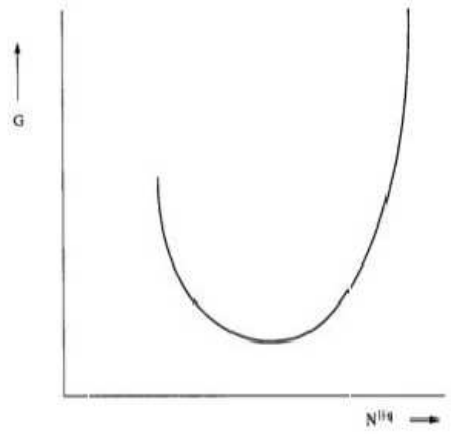

Fig. 12. Gibbs energy versus N^{liq} in an alloy shown schematically.

This process is repeated until the Gibbs energy is minimized. The same procedure is then applied by varying the amount and composition of the first phase as shown in Fig. 14(a).

This cycle is repeated as shown in Fig. 14(b) and 14(c) until a minimum is obtained in the Gibbs energy and the convergence criteria is satisfied.

3. Stepping and mapping

The previous procedures are for the calculation of equilibrium points at specific composition, temperature and pressure. However, for phase diagram calculations when changing a particular condition, such as composition or temperature in the present case, a procedure known as stepping is employed. In this process, the property is in-

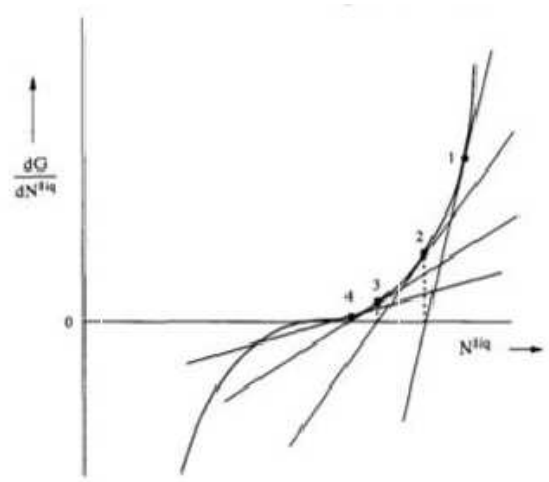

Fig. 13. Calculation of the second derivative of G with respect to N^{liq} to obtain the minimum in Gibbs energy.

creased in small amounts or steps, and then the stability of the phase is checked at this step. If the phase is stable at that particular step, it is used as a starting point for the next step. This process is repeated until the conditions are not satisfied. Mapping is the process by which a phase diagram is plotted and employs the calculated results of the stepping code to map a phase boundary. Binary phase diagrams have two degrees of freedom that are most commonly represented by the temperature and composition.

The requirements from a calculation method must be to: reduce the degrees of freedom, calculate the Gibbs energy of the system and, use some iterative technique to minimize the Gibbs energy. Also, the robustness and the speed of the calculations depend heavily on the choice of starting guesses for the model parameters. Even though the calculation methods being used might be global minimization programs, there is always a possibility for the calculation to get stuck at a local minimum and thus giving an incorrect equilibrium result. Hence, it is always recommended to have

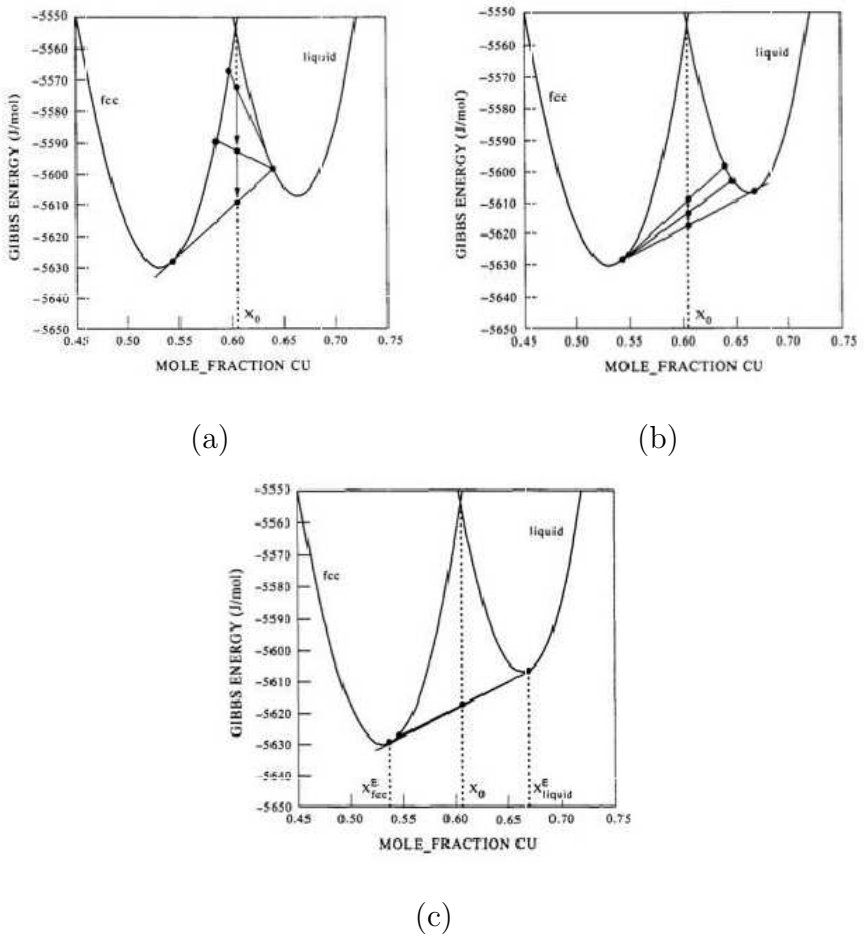

Fig. 14. Second, third, and fourth stage in the iteration process of Gibbs energy minimization of a Cu-Ni alloy with composition x_0 in Cu, and at 1523 K [17].

some prior knowledge of the phase diagram equilibria. This problem is most evident in the case of phases that have a miscibility gap. In case of availability of prior information on the miscibility information, such a phase is then given start points for both #1 and #2 phases by the program and it ensures the convergence accounts for both minima. In the present work, a similar approach is followed for the bcc phases where two sets, BCC#1 and BCC#2 are introduced in the system. However, in a generalized environment, this method would fail if unknown miscibility gaps were

present or if there was an order/disorder transition associated with the phase. Thus, some prior knowledge of miscibility gap or ordering is necessary to obtain reasonable accuracy and speed of execution.

4. The PARROT programme

The PARROT module [56] is integrated with the Thermo-Calc package [57] and is essentially based on the following governing principles:

- Establish a criterion for best fit: This criterion is based on a maximum likelihood principle where a likelihood function is chosen and must be maximized to obtain the best estimates of the model parameters. Simplification of this process is made by assuming that the joint probability density function of all the experimental data is Gaussian in form and, that there is no dependence or coupling between different experimental measurements.

- Data separation based on accuracies: The PARROT module allows the user to input experimental data that are significantly inaccurate compared with their true values in addition to the data which are free from such inaccuracies. Dependent and independent variables: Both types of variables can be used in the optimization process of the PARROT module. Dependent variables are those that describe the responses of the system to prescribed conditions whereas, independent variables define the equilibrium conditions. The calculation of the Gibbs energies for different phases and the determination of equilibria are then performed by the Poly-3 module of the Thermo-Calc software that is coupled with PARROT. State variables such as temperature, pressure and chemical potentials, are treated as independent variables and are preselected to define the equilibrium conditions. Dependent variables, or re-

sponses of the system, are then written as functions of the independent variables and the model parameters. This makes it possible to use almost any type of experimental information in the evaluation of the model parameters. A significant advantage of using the CALPHAD method is that various other properties can be automatically obtained after the calculation procedure and can also be plotted as functions of the state variables.

In the present work on the Np-Zr system, as the experimental information available sometimes contradict one another, particularly while defining the nature of the bcc phase, the optimization process was started with a small number of iterations and very low statistical weights assigned to the experimental data. The bcc phase was optimized in such a way that no preference was given whatsoever to any information determining its character, miscible or immiscible. The weights were increased appropriately during the optimization process to be within an acceptable range of experimental data. To aid in the calculation of a global equilibrium, another constraint that was used was the driving force for the formation of a particular phase. Driving force is defined as the affinity between reacting chemical species, and its magnitude gives the equilibrium of a phase at particular composition and temperature. At particular temperature and composition it is negative for the stable phase, and positive for the phases that are not at equilibrium under those conditions. Also, the optimization was carried out until a balance was achieved between different sets of input data, which in the present work are the solidus, liquidus equilibrium lines and the formation enthalpies of the bcc phase.

CHAPTER IV

ELECTRONIC STRUCTURE CALCULATIONS

A. Introduction

Density Functional Theory (DFT) has been a popular method for the quantum mechanical solution of periodic systems, and to compute the electronic structure of matter. It was proven to be a very successful approach for the description of ground-state properties of metals, semiconductors, and insulators. In this section, a brief formulation of this method is described.

Consider a solid of atomic number Z, and composed of N number of nuclei. These nuclei are positively charged particles and heavier than the negatively charged electrons. The total number of interacting particles in such a solid becomes (N + ZN), thus making this a many-body problem. The Hamiltonian for a solid is given by,

$$\begin{aligned}\hat{H} &= -\frac{\hbar}{2}\sum_i \frac{\nabla^2_{\overrightarrow{R}_i}}{M_i} - \frac{\hbar}{2}\sum_i \frac{\nabla^2_{\overrightarrow{r}_i}}{m_e} \\ &\quad - \frac{1}{4\pi\epsilon_0}\sum_{i,j}\frac{e^2 Z_i}{\mid \overrightarrow{R}_i - \overrightarrow{r}_j \mid} + \frac{1}{8\pi\epsilon_0}\sum_{i\neq j}\frac{e^2}{\mid \overrightarrow{r}_i - \overrightarrow{r}_j \mid} \\ &\quad + \frac{1}{8\pi\epsilon_0}\sum_{i\neq j}\frac{e^2 Z_i Z_j}{\mid \overrightarrow{R}_i - \overrightarrow{R}_j \mid}\end{aligned} \tag{4.1}$$

where, the nuclei are of mass M_i and at $\overrightarrow{R_i}$, and the electrons are of mass m_e and at positions $\overrightarrow{r_i}$. The first two terms are the kinetic energy operators of the nuclei and electrons, respectively. The last three terms describe the Coulombic interactions between a nucleus and an electron, between two electrons, and between two nuclei, respectively.

Even for the modern-day computers, it is extremely challenging to solve (4.1) exactly for elements with more than a few electrons. Thus, several approximations are made to ease the calculations. These are briefly described in the following subsections.

1. The Born-Oppenheimer Approximation

This approximation assumes the nuclei to be "frozen" due to their heavier masses. Thus, the kinetic energy term of the nuclei is eliminated, and the potential term now becomes a constant. Thus, only electrons are left as interacting particles in this many-body problem, and (4.1) reduces to,

$$\hat{H} \;=\; \hat{T} \;+\; \hat{V} \;+\; \hat{V}_{ext} \tag{4.2}$$

where the first term ($\hat{T}$) is the kinetic energy operator for the electrons, the second term ($\hat{V}$) describes the potential energy between the electrons, and the last term ($\hat{V}_{ext}$) is the potential energy of the electrons in the external potential of nuclei.

2. Density Functional Theory

After the first level of approximations, the problem becomes simpler, but still remains difficult to solve. Thus, the so-called Density Functional Theory (DFT) is used to simplify the problem further and this method relies on two important theorems by Hohenberg and Kohn [58]. The first theorem states that there is a one-to-one relationship between the external potential V_{ext} and the ground-state density $\rho(\overrightarrow{r})$ of a many-electron system. The second theorem gives the ground-state total energy functional $H[\rho] \;\equiv\; E_{V_{ext}}[\rho]$ as,

$$E_{V_{ext}}[\rho] \;=\; \underbrace{<\psi|\hat{T} \;+\; \hat{V}|\psi>}_{F_{HK}[\rho]} \;+\; <\psi|\hat{V}_{ext}|\psi> \tag{4.3}$$

where the Hohenberg-Kohn density functional $F_{HK}[\rho]$ is universal for many-electron systems as it contains information regarding only electrons and not protons. It is postulated in this theorem that at the ground-state density V_{ext}, the ground-state energy functional $E_{V_{ext}}[\rho]$ reaches its minimum value.

3. Kohn-Sham equations

The Kohn-Sham equations helped turn DFT into a usable and practical tool. The first formulation is defined for the correlation energy which is the part of the total energy present in the exact solution, but absent in the Hartree-Fock solution, and is given by,

$$V_c \;=\; T \;-\; T_0 \tag{4.4}$$

where T is the exact kinetic energy functional for the electrons, and T_0 is the kinetic energy functional for a non-interacting electron gas.

The second formulation defines the exchange contribution to the total energy that is present in the Hartree-Fock solution, and absent in the Hartree solution. Thus, it is given by,

$$V_x \;=\; V \;-\; V_H \tag{4.5}$$

where V is the exact electron-electron potential energy functional, and V_H is the Hartree contribution.

Thus, the Hohenberg-Kohn functional, from (4.3) is written in the following way,

$$\begin{aligned} F_{HK} &= T + V + T_0 - T_0 \\ &= T_0 + V + (T - T_0) \\ &= T_0 + V + V_c && \text{from (4.4)} \\ &= T_0 + V_H + V_c + (V - V_H) \\ &= T_0 + V_H + V_c + V_x && \text{from (4.5)} \end{aligned}$$

where V_{xc} is the exchange-correlation energy functional. The energy functional is thus written as,

$$E_{V_{ext}}[\rho] = T_0[\rho] + V_H[\rho] + V_{xc}[\rho] + V_{ext}[\rho] \tag{4.6}$$

The corresponding Kohn-Sham Hamiltonian is given by,

$$\hat{H}_{KS} = \hat{T}_0 + \hat{V}_H + \hat{V}_{xc} + \hat{V}_{ext} \tag{4.7}$$

The eigenstates are then determined by solving a Schrödinger-like non-interacting single-particle equations given by,

$$\hat{H}_{KS}\phi_i = \epsilon_i\phi_i \tag{4.8}$$

Since both V_H and V_{xc} depend on the electron density $\rho(\overrightarrow{r})$, which in turn depends on the wavefunctions ϕ_i being calculated, this problem becomes self-consistent. In the first step, an initial guess of the electron density density ρ_0 is made. With this value, the Hartree operator V_H and exchange-correlation operator V_{xc}, both of which

depend on ρ_0, are calculated. Thus, the Hamiltonian H_{KS} is constructed, and the eigenvalue problem is solved to obtain ϕ_i which in turns leads to the calculation of a new density ρ_1. This new density is then compared with the starting guess ρ_0, and the procedure is repeated again until both become equal.

B. Local Spin Density Approximation

The exchange-correlation functional V_{xc} can be approximated within the Local Spin Density Approximation (L(S)DA) [59]. In this approximation, the material is divided infinitesimally into small volumes, with each volume contributing to the total exchange correlation energy by an amount equal to that of an identical volume filled with a homogeneous electron gas that has the the same density. The exchange-correlation energy functional by this method is given by,

$$E_{xc}^{LSDA} = \int \rho(\overrightarrow{r})\epsilon_{xc}(\rho(\overrightarrow{r}))d\overrightarrow{r} \tag{4.9}$$

C. Generalized Gradient Approximation

In this method, the exchange-correlation contribution of every infinitesimal volume not only depends on that volume, but also on the density in neighboring volumes [60]. Thus, the gradient in density between different volumes is also taken into account, and thus it is termed as Generalized Gradient Approximation (GGA).

D. Solving the Kohn-Sham equations

The single-electron equations to solve are infinite and similar to eqn.(4.8) irrespective of the method of approximation chosen for the exchange-correlation functional. The wave functions are expressed as,

$$\phi_m \;=\; \sum_{p=1}^{P} c_p^m \phi_p^b \tag{4.10}$$

where c_p^m are the coefficients to be calculated, and ϕ_p^b is a basis set. The dimensions of the function space in which the wave functions ϕ_m are being searched, are infinite, thus making P infinite. However, it is impossible to work with an infinite basis set, and thus, its selection is made in such a way that the resulting functions are close to ϕ_m. Larger the value of P, the more accurate are the wave functions, but more time consuming are the calculations. Once the selection of a basis set is made, solving eqn.(4.8) becomes an eigenvalue problem. The choice of a basis set is made in such a way that it is both efficient, i.e. it represents the wave functions as closely as possible thus requiring lower values of P, and unbiased, i.e. its properties are not influenced by the wave functions. One such basis set that satisfies both of these requirements quite well is the plane wave basis set which is briefly described in the following section.

E. Pseudo-potential method

Bloch's theorem defines an eigenfunction as,

$$\psi_{\overrightarrow{k}}^{n}(\overrightarrow{r}) \;=\; \sum_{\overrightarrow{K}} c_{\overrightarrow{K}}^{n,\overrightarrow{k}}\, e^{i\,\overrightarrow{k}\,.\,\overrightarrow{r}} \tag{4.11}$$

where $c_{\overrightarrow{K}}^{n,\overrightarrow{k}}$ are coefficients to be determined, $e^{i\,\overrightarrow{k}\,.\,\overrightarrow{r}}$ is a plane wave that contains the periodicity of the lattice, and $\overrightarrow{k}$ is a vector in the first Brillouin zone. Comparing equations (4.10) and (4.11), we thus obtain that m represents $(n,\, \overrightarrow{k})$, and p represents $(\overrightarrow{k} \;+\; \overrightarrow{K})$.

However, such a basis set is also almost impossible to calculate accurately. Thus,

the potential in regions close to the nuclei, which is its most fluctuating part, is replaced by a pseudo-potential that yields smooth wavefunctions near the atomic nucleus as this part of the solid behaves similarly to free atom electrons. This makes the basis set manageable to calculate for a system.

F. L(S)DA+U method

The Local Spin Density Approximation (L(S)DA) method often fails to describe the energetics and ground-state properties of strongly correlated and highly localized d and f electron systems, such as in the case of Np in the present work. Such systems usually contain transition metal or rare-earth metal ions with partially filled d (or f) shells. When applying a one-electron method with an orbital-independent potential, like in the LDA, to transition metal compounds, the result is a partially filled d-band with metallic type electronic structure and itinerant d-electrons. This is an incorrect result for late-transition-metal oxides and rare-earth metal compounds where d(f) electrons are well localized and there is a sizeable energy separation between empty and filled bands [61].

Thus, within the L(S)DA method, electrons are separated into two subsystems: one with delocalized s,p electrons which could be described by using an orbital-independent one-electron potential (LDA), and the other with localized d or f electrons for which Coulomb d-d interaction should be taken into account by a term $\frac{1}{2}\mathrm{U}(\mathrm{n}_i\mathrm{n}_j)$ ($\mathrm{i}\neq\mathrm{j}$) as in a mean-field (Hartree-Fock) approximation. Thus, the L(S)DA energy function is modified by introducing a term that includes strong intra-atomic interaction in a (screened) Hartree-Fock like manner. This defines the Dudarev formulation [62] of the L(S)DA + U method in which case the functional is written as,

$$E_{L(S)DA+U} \;=\; E_{L(S)DA}[\epsilon_i] \;+\; \frac{(U \;-\; J)}{2} \sum_{l,j,\sigma} \rho^{\sigma}_{lj} \rho^{\sigma}_{jl} \tag{4.12}$$

where U and J are model parameters which must be carefully chosen when comparing with experimental data, ϵ_i are the Kohn-Sham eigenvalues, ρ^{σ}_{lj} is the density matrix of electrons occupying a partially filled electron shell, and σ gives the spin direction. In this approach, only the difference $U_{eff} \;=\; (U \;-\; J)$ is meaningful rather than the individual parameters U and J.

G. KKR-ASA-CPA method

Formation enthalpies of bcc alloys at various compositions were computed using a scalar-relativistic Green function technique based on the Korringa-Kohn-Rostoker (KKR) method within the atomic sphere approximation (ASA) [63–65], which is improved by addition of higher multipoles of the charge density [65], and the so called muffin-tin correction [66] to the electrostatic energy. The Generalized Gradient Approximation (GGA) is adopted to approximate the electron exchange and correlation energy functional. To treat compositional disorder the KKR-ASA method is combined with the Coherent Potential Approximation (CPA) [67] . More details of this approximation can be found in Ref. [12].

CHAPTER V

RESULTS AND DISCUSSION

A. Lattice stabilities

Thermodynamic models for the Np-Zr system have been developed in a way that they can be validated with any sets of thermodynamic data that is either already available or, can be calculated using first-principles techniques. And one such data set that is calculated in the present work is lattice stabilities.

One of the main requirements of the CALPHAD method is the calculation of the Gibbs energy versus composition for all the phases exhibited by the elements and the alloy system. This condition is met only when the Gibbs energies of phases can be calculated in the unstable or metastable regions of those phases in the temperature-composition space. Thus, the Gibbs energy of the elements in all their potential crystal structures must be calculated and the relative differences in the energies between these phases are refered to as lattice stabilities.

In the present work, the lattice stabilities are calculated, using the VASP code, by subtracting total energies of the pure elements in their reference states (Np:orthorhombic, Zr:hcp), from the energies of both elements in their corresponding unstable crystal structures (Np in hcp phase, Zr in orthorhombic and tetragonal phases). The calculations are performed within both LDA and GGA methods, and the the values obtained are found to lie within these limits. In Table II, they are compared with those obtained from our thermodynamic model, and with the ones evaluated in the case of U-Zr alloy system [18].

Table II. Lattice stabilities obtained from *ab initio* calculations within the LDA and GGA methods, compared with values from the thermodynamic model developed in the present work and with case of the U-Zr alloy system [18].

Element	Phase	Space Group	LDA (J/mole)	GGA (J/mole)	Model (J/mole)	U-Zr [18] (J/mole)
Np	Hcp	$P6_3/mmc$	74860.61	49106.39	70000	–
U	Hcp	$P6_3/mmc$	–	–	–	50000
Zr	Orthorhombic	Pnma	1613.97	5680.87	5837.36	38000
Zr	Tetragonal	P4/nmm	1688.53	5630.14	4056.09	35000

B. Phase diagram

The parameters, that are used to construct the Gibbs energy expressions of all the phases in the system, are optimized using the minimization procedure implemented within the PARROT program, until the deviations from the experimental input are reduced to a minimum. The final values of these parameters are listed in Table III, and the Gibbs energy expressions used for all the phases of both elements along with their standard element reference state (SER) are given in detail in Appendix A. The phase diagram calculated from these optimized parameters (Model 1) is shown in Fig. 15, where it is compared with the postulated phase diagram published by Gibson *et al.* [8], along with DTA peaks obtained for various alloys from Ref. [7].

It is clear that the calculated phase diagram is in agreement with most of the phase equilibria predicted by Gibson *et al.* [8]. The discrepancies are limited to the positions of the liquidus, solidus, and, bcc/hcp equilibrium lines. These disagreements can be explained as follows. A stage was reached during the optimization process where a compromise had to be made between the calculated formation en-

Table III. Model description and optimized parameters for all the different phases in the Np-Zr system (Va=Vacancy).

Phase	Model	Evaluated parameters (J/mole)
Liquid	Random Solution $(Np,Zr)_1$	${}^0L^{Liq}_{Np,Zr} = 126720.48 - 122.25 * T$
		${}^1L^{Liq}_{Np,Zr} = 27741.16 - 48.36 * T$
bcc	Sublattice model $(Np,Zr)_1(Va)_3$	${}^0L^{bcc}_{Np,Zr:Va} = 95381.69 - 84.08 * T$
		${}^1L^{bcc}_{Np,Zr:Va} = 83326.26 - 87.96 * T$
		${}^2L^{bcc}_{Np,Zr:Va} = -1133.70 - 12.25 * T$
hcp	Sublattice model $(Np,Zr)_1(Va)_{0.5}$	${}^0G^{hcp}_{Np:Va} - {}^0G^{ort}_{Np} = 70000$
		${}^0L^{hcp}_{Np,Zr:Va} = -48071.49 - 6.75 * T$
ortho	Random Solution $(Np,Zr)_1$	${}^0G^{ort}_{Zr} - {}^0G^{hcp}_{Zr} = 5837.36 - 2.64 * T$
		${}^0L^{ort}_{Np,Zr} = -2528.41 + 35.95 * T$
tetra	Random Solution $(Np,Zr)_1$	${}^0G^{tet}_{Zr} - {}^0G^{hcp}_{Zr} = 4056.09 + 1.36 * T$
		${}^0L^{tet}_{Np,Zr} = -3356.11 + 30.50 * T$
θ	Sublattice model $(Np)_4(Zr)_1$	${}^0G^{\theta}_{Np:Zr} - 4{}^*{}^0G^{ort}_{Np} - {}^0G^{hcp}_{Zr} = -2250.09 + 0.09 * T$
δ (Model 1)	Sublattice model $(Np,Zr)_2(Zr)_1$	${}^0G^{\delta}_{Np:Zr} - 2{}^*{}^0G^{ort}_{Np} - {}^0G^{hcp}_{Zr} = 2438.4 + 0.7 * T$
		${}^0G^{\delta}_{Zr:Zr} - 3{}^*{}^0G^{\omega}_{Zr} = 1800$
		${}^0L^{\delta}_{Np,Zr:Zr} = -9836.28 + 28.54 * T$
		${}^1L^{\delta}_{Np,Zr:Zr} = 3135 - 4.88 * T$
δ (Model 2)	Sublattice model $(Np,Zr)_2(Zr)_1$	${}^0G^{\delta}_{Np:Zr} - 2{}^0G^{ort}_{Np} - {}^0G^{hcp}_{Zr} = 28330.9 - 28.1 * T$
		${}^0G^{\delta}_{Zr:Zr} - 3{}^*{}^0G^{\omega}_{Zr} = 0$
		${}^0L^{\delta}_{Np,Zr:Zr} = -69268.56 + 101.48 * T$
		${}^1L^{\delta}_{Np,Zr:Zr} = -44401.87 + 48.11 * T$

thalpies of the bcc phase (explained later on), which was one of the thermodynamic constraints applied to the system, and, these equilibrium lines. In addition, no peaks were observed above 913 K from DTA experiments [7].

In Fig. 16 the calculated phase diagram (Model 1) is compared with dilatometry and EPMA results obtained by Rodríguez *et al.* [11]. In Ref. [68], it is explained that the probability of melting points of (γ-Np,β-Zr) measured by Rodríguez *et al.* [11] corresponding to the Liquid + β-Zr liquidus in the non-ideal phase diagram, is highly probable. This reasoning is compatible with the phase diagram in Fig. 16.

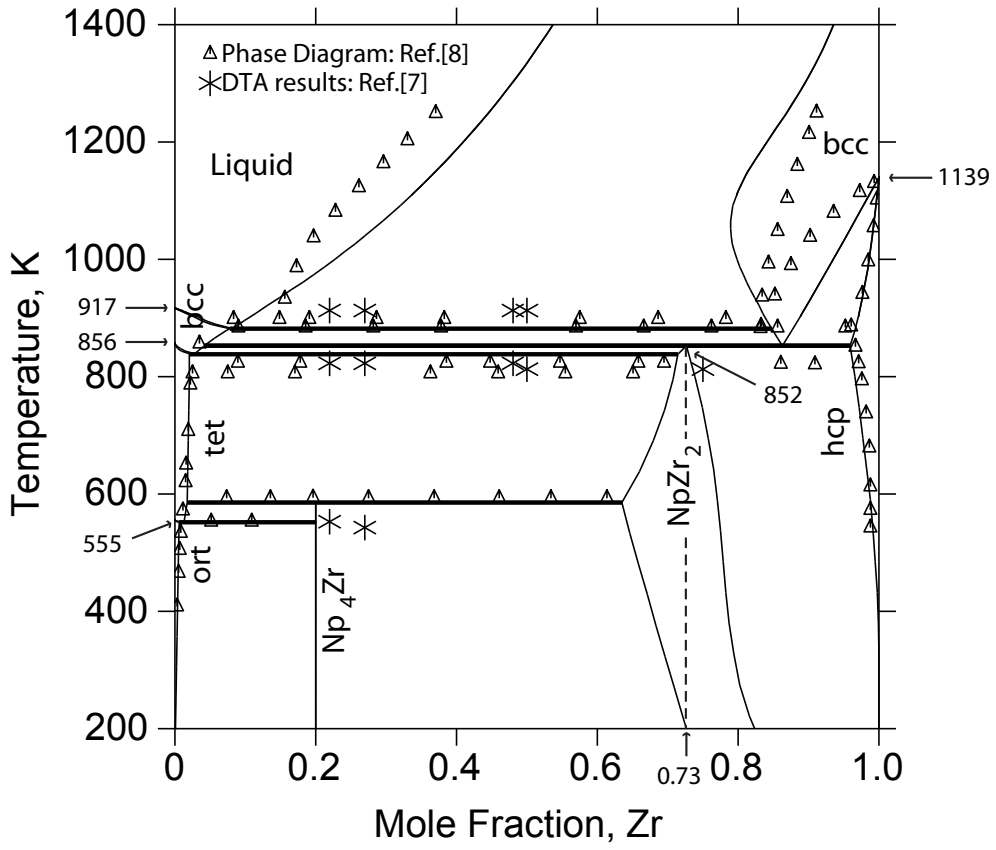

Fig. 15. Calculated Np-Zr phase diagram - Model 1, compared with the postulated phase diagram displayed in Ref. [8], and the DTA results from Ref. [7].

As it has been asserted several times [8, 16] that the Np-Zr phase diagrams previously published are speculative and, given the scarcity of experimental data points available, the inconsistencies between the calculated phase diagram and those published earlier can be ignored to some extent. The temperatures and compositions of the calculated and reported invariant reactions are shown in Table IV, and are in good agreement with each other.

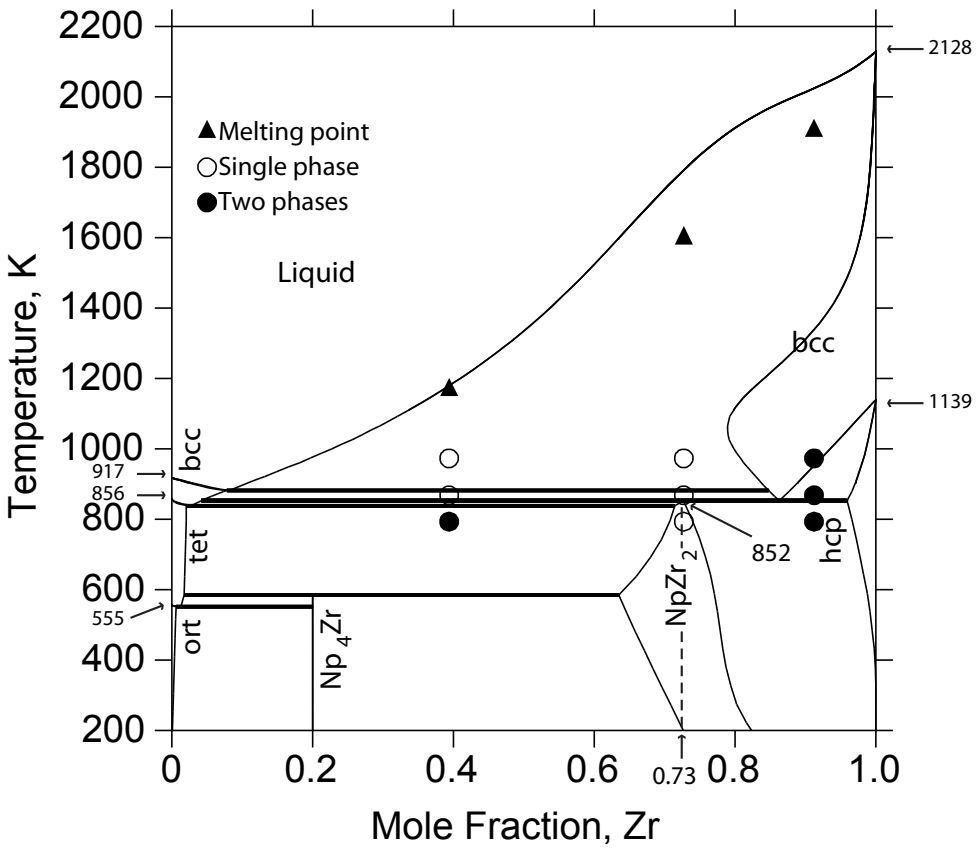

Fig. 16. Calculated Np-Zr phase diagram- Model 1, compared with dilatometry and EPMA data from Ref. [11].

The resulting Np-Zr phase diagram was obtained with a miscibility gap in the bcc phase, thus conforming the postulations made in Refs. [6–10, 16]. To study the effect of atomic structure and bonding properties on the nature of bcc solid solution in the U-Zr, Np-Zr, and Pu-Zr systems, a comparison between metallic radii, electronegativities and cohesive energies was made in Ref. [7]. Since, the metallic radii and electronegativities of Np and Zr are very similar, it would be anticipated that the bcc solid solution would exhibit continuous miscibility, like in the U-Zr and Pu-Zr

Table IV. Invariant reactions in the Np-Zr system

Reaction	H. Okamoto [69]		Present work		Reaction type
	x (Zr)	Temp (K)	x(Zr)	Temp (K)	
L $\rightarrow$ γ-Np + β-Zr	0.15	903	0.08	882	Eutectic
β-Zr $\rightarrow$ γ-Np + α-Zr	0.83	883	0.86	852.3	Eutectoid
γ-Np + α-Zr $\rightarrow$ δ-$NpZr_2$ (Model 1)	0.70	823	0.73	852.2	Peritectoid
γ-Np + α-Zr $\rightarrow$ δ-$NpZr_2$ (Model 2)	0.70	823	0.79	843.5	Peritectoid
γ-Np $\rightarrow$ β-Np + δ-$NpZr_2$	0.03	803	0.03	838.5	Eutectoid
β-Np + δ-$NpZr_2$ $\rightarrow$ θ-Np_4Zr	0.20	588	0.20	585.5	Peritectoid
β-Np $\rightarrow$ α-Np + θ-Np_4Zr	0.015	553	0.015	551	Eutectoid

systems. However, it was noticed that the contribution of 5f orbital bonding to the cohesive energy was maximum in case of Np (about 3 times of U and 1.5 times of Pu) [7, 8]. The implications of this result is that when a non-5f bonded element such as Zr is alloyed with a f-electron element such as Np, it results in a larger disruption in 5f bonding which explains the resistance to mixing and the resulting immiscibility.

Recently, Kurata [70] calculated the Np-Zr phase diagram with complete solid solubility of the bcc phase, similar to the characteristic of the bcc phase in the U-Zr and Pu-Zr systems. This result was based on the assumption that interaction parameters of the bcc phase in both Np-Zr and Pu-Zr, should almost be the same. This assumption may not necessarily be true and, it is unlikely that the nature of chemical reaction in both systems will be similar or that the bcc phase will from complete miscible solid solutions.

C. The bcc phase

Another set of thermodynamic data that is used to optimize and validate the calculation of the Np-Zr phase diagram is the set of formation enthalpies of the bcc phase. These values are obtained as functions of composition from electronic structure cal-

culations using the KKR-ASA-CPA method, and are compared with those obtained from the calculated thermodynamic model in Fig. 17. High positive values are a proof of the tendency towards phase separation in these alloys, thus confirming our results.

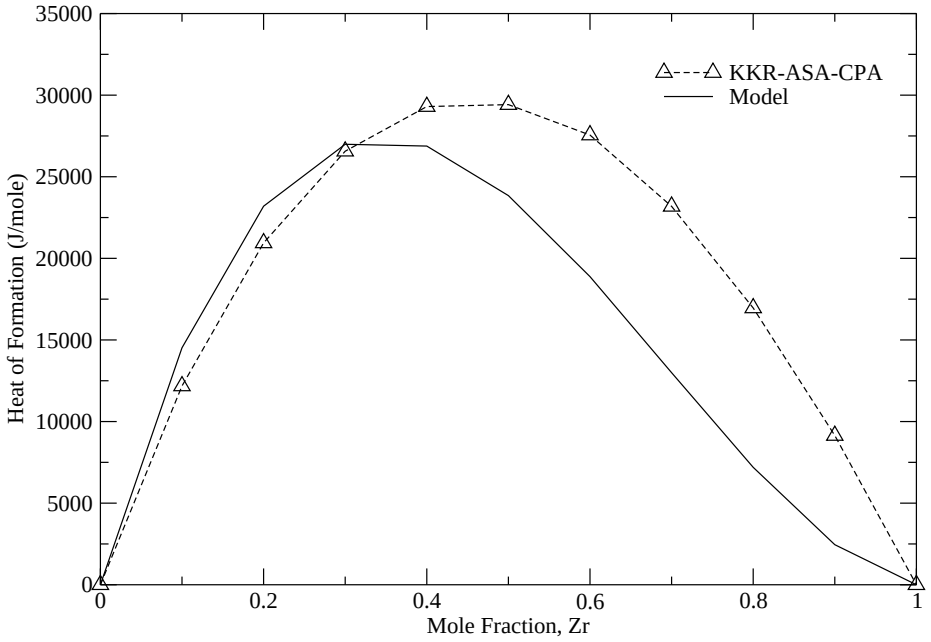

Fig. 17. Calculated formation enthalpies of the bcc-based Np-Zr alloys obtained from the thermodynamic model compared with results from first-principles electronic structure KKR-ASA-CPA calculations within the GGA approximation.

The KKR-ASA-CPA code is also used to calculate atomic volumes and bulk moduli of bcc-based Np-Zr alloys as functions of composition which are plotted in Fig. 18. This plot also shows the linear variation between values obtained for pure bcc-Np and bcc-Zr, that would be expected based on Zen's Law [71]. Positive deviation in volumes and negative deviation in bulk moduli confirms the resistance in

bonding between Np and Zr and thus, resulting in a miscibility gap in the bcc phase.

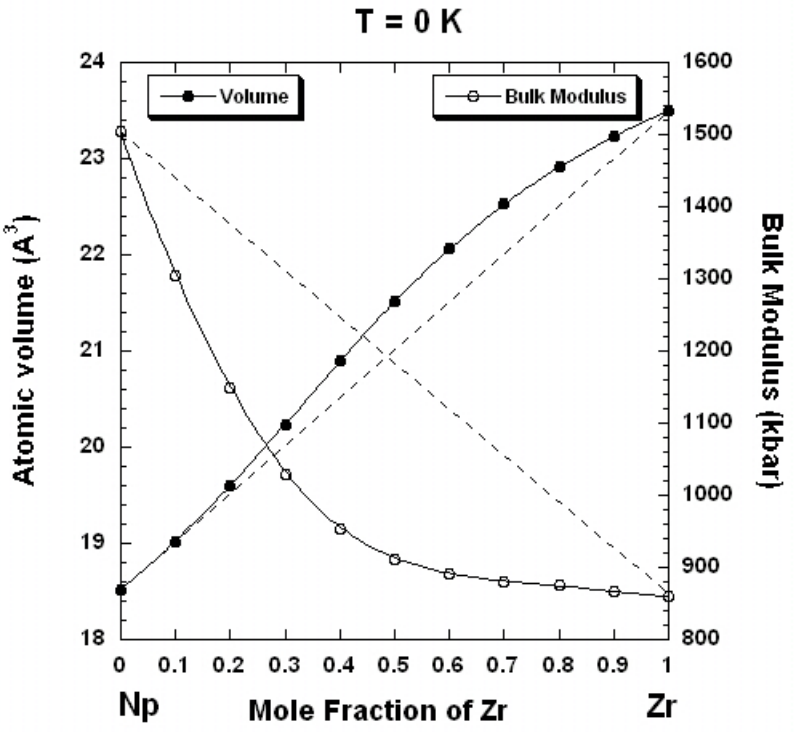

Fig. 18. Atomic volume and bulk modulus of bcc-based Np-Zr alloys calculated as functions of composition using the KKR-ASA-CPA method. Dotted lines denote the expected linear relationship based on Zen's Law [71].

D. The δ-$NpZr_2$ phase

In Chapter II it was explained that as the d-band occupation of Zr increases when alloying with actinides, the stability of the C32 structure increases, which is the case in alloys of U and Np [12]. A similar behavior is expected to be responsible for the stability of the δ-phase in the Np-Zr system. In the present work, this phase is modeled as a two-sublattice phase. One of the sublattices contains two sites, namely the $(\frac{2}{3}, \frac{1}{3}, \frac{1}{2})$ and $(\frac{1}{3}, \frac{2}{3}, \frac{1}{2})$ positions, that are occupied by a random mixture of Np and Zr

atoms. The second sublattice contains just one site, the (0, 0, 0) position, which is occupied by Zr atom. This configuration results in a $(Np,Zr)_2(Zr)_1$ configuration, which is similar to the one proposed for the δ-UZr_2 phase. From first-principles calculations [12], it was found that this configuration has the lowest energy out of all possible configurations resulting from the distribution of atoms on the sites of this structure. The decomposition of this phase into a mixture of γ-Np and α-Zr is assumed to take place at about 823 K, which is in accordance with the findings of Refs. [6, 7, 9]. The composition range over which the δ-phase extends was found to be from 65.3 to 78.2 at.% Zr [11].

In Fig. 19 the molar Gibbs energy of formation of the δ-phase is plotted as a function of composition at 840 K as calculated from the model. The minimum of this curve occurs at a Gibbs energy of about -1 kJ/mole. From calorimetry measurements [72, 73], formation enthalpy of the δ-UZr_2 phase is found to be -4.0 kJ/mole and, from first-principles calculations it is found to be -6.289 kJ/mole [12]. In comparison with the Pu-Zr system, the δ-phase does not become stable, and thus does not take part in the phase equilibria of the system [47, 48]. This decrease of stability, when going from U to Np and then to Pu, is expected and conforms with the calculations in Ref. [12] where it was shown that the critical d-band occupation change needed to form the δ-phase was reached for a lower concentration of U than Np when alloying with Zr, thus resulting in a relatively higher energy for formation in the Np-Zr system in comparison with the U-Zr system. Whereas, in the case of Pu, the d-band occupation change always remained lower than the critical value, thus explaining the absence of the δ-phase in the Pu-Zr phase diagram.

The stabilities/instabilities of the hcp and ω-phases of pure Zr are compared in

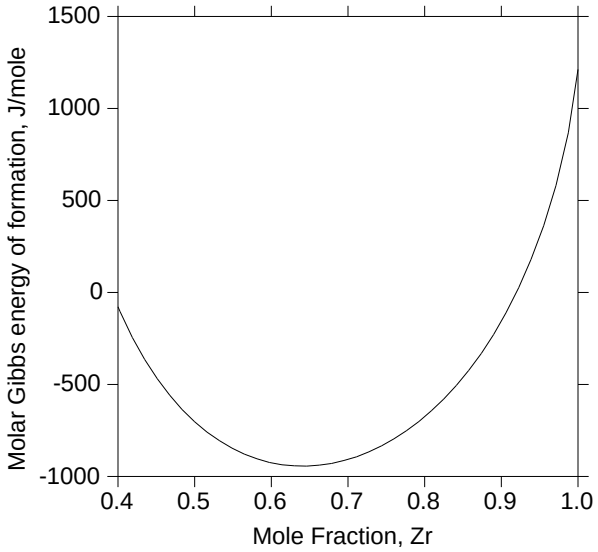

Fig. 19. Calculated molar Gibbs energy of formation of the δ-phase as a function of composition at 840 K, with the orthorhombic and hexagonal phases as reference states for Np and Zr, respectively.

Fig. 20, which shows the Gibbs energy of these two phases as a function of temperature as retrieved from the SGTE database. In this plot, it can be seen that the energy curve of the ω-structure is lower than that of hcp up to about 230 K, beyond which it crosses over, and thus becomes unstable above this temperature. However, the Gibbs energy description (as obtained from the SGTE database) of the ω-phase is defined above 298 K, whereas that for the hcp phase is defined above 130 K. Thus, below 298 K, the energy curve for the ω-phase in Fig. 20 is obtained by mere extrapolation, and the question of the more stable phase for Zr remains unanswered.

Due to this, a value of 600*3 J/mole (3 for the total number of sites) was added to the Gibbs energy description of the ω-structure in the δ-phase, i.e. ${}^{0}G^{\delta}_{Zr:Zr} - 3{}^{*0}G^{\omega}_{Zr}$, in Model 1. And, in Model 2, no such modification was made and thus, the ω-phase was more stable than the hcp phase at low temperatures. Thus, the phase diagram

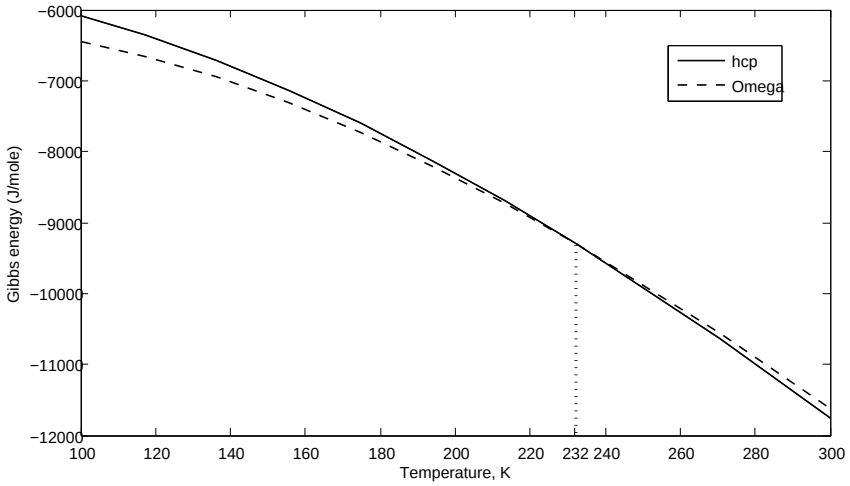

Fig. 20. Gibbs energy versus temperature for the hcp and ω-phases of pure Zr showing a change of stability at about 232 K.

calculated in this case is shown in Fig. 21. As expected, a miscibility gap is formed in the δ-phase. The second part of this phase forms nearly at x(Zr)=1 and represents the ω-phase of pure Zr. Fig. 22 shows the low-temperature Zr-rich region of the phase diagram.

Future experimental works that may be conducted to resolve important issues in the Np-Zr phase diagram, such as the miscibility/immiscibility of the bcc phase, and stability range of the δ-phase, can be guided by providing thermodynamic information that would be expected to be seen in this system. Thus, the molar enthalpies of the system at temperatures within the range of 700-1000 K, are calculated and plotted for two alloy compositions, 73 and 86 at.% Zr in Fig. 23. Both compositions are Zr-rich which would make the preparation of such samples slightly easier than Np-rich samples, which poses limitations not only due to its radioactive nature, but also due to the difficulty in obtaining access to it for conducting experiments. As expected, a sudden increase in enthalpy ($\sim$10-15 kJ/mole) is seen in Fig. 23 at around the phase

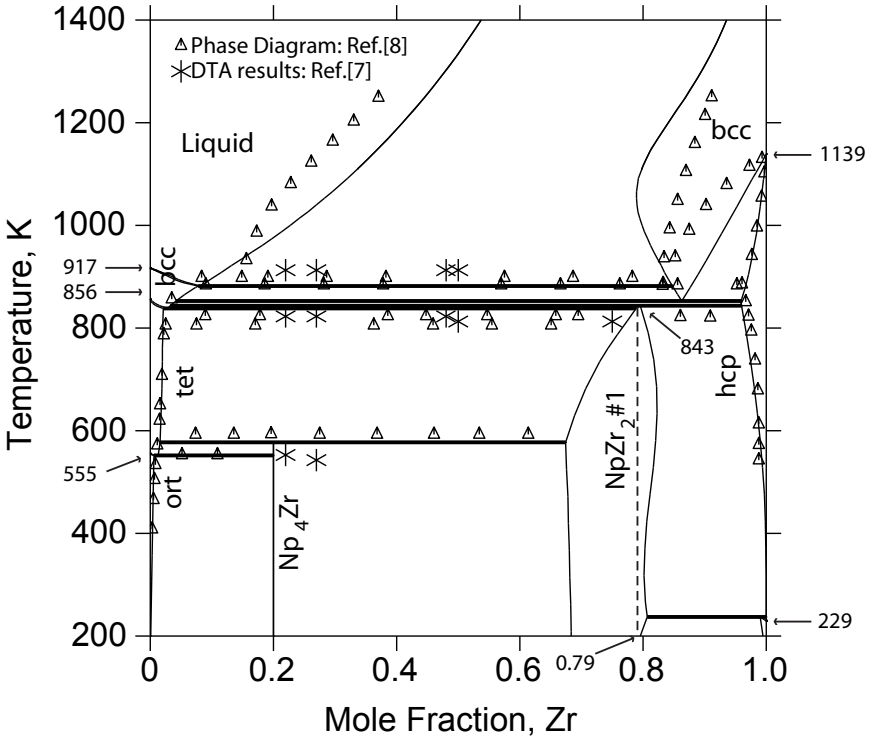

Fig. 21. Calculated phase diagram- Model 2 showing the miscibility gap in the δ-$NpZr_2$ phase, compared with phase diagram information from Ref. [8] and DTA results from Ref. [7].

transition temperatures ($\sim$850^{o}K) for both alloys.

E. L(S)DA+U study of pure Np

All the calculations in this work were performed using the VASP package [74–77]. The ion-electron interactions were described using the projector augmented-wave (PAW) method [78–80] which helps in reducing the number of plane-wave basis functions needed to describe the electronic wave functions accurately. The PAW potential was generated considering the $6d$, $7s$, and $5f$ electrons as valence states for Np, and the

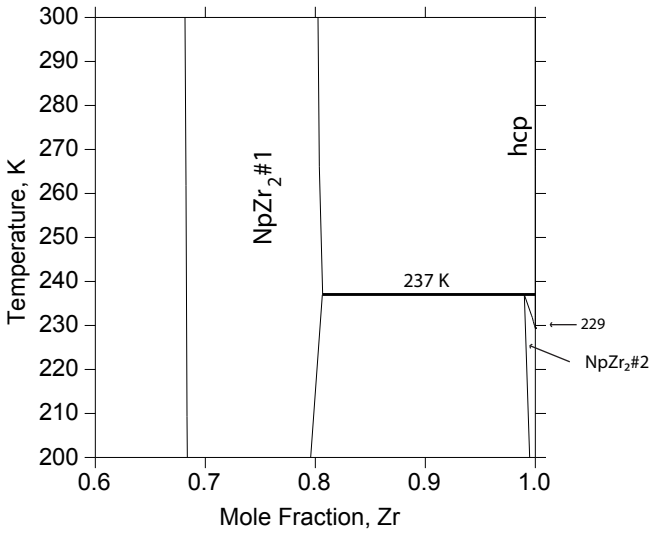

Fig. 22. Low-temperature and Zr-rich section of the calculated phase diagram- Model 2 showing the stability of the ω-phase ($NpZr_2$#2) over the hcp phase below 237 K, and a miscibility gap between δ-$NpZr_2$#1 and $NpZr_2$#2.

$4s$, $4p$, $4d$, and $5s$ electrons for Zr. First, calculations were performed, for both Np and Zr, using local (spin-) density approximation (L(S)DA) for the exchange-correlation functional, to relax all ions in the structure by changing the cell shape and volume. Then, due to the effects of high localization and strong correlations among the f-electrons in Np, the L(S)DA+U formalism is used to approximate the exchange-correlation energy. In the latter case, we adopted the simplified rotationaly invariant method proposed by Dudarev *et. al* [62], in which the total energy only depends on U_{eff}, which is the difference between the Coulomb, U, and exchange, J, parameters. In the present study, the value of U is varied, but J is fixed at $J = 1\ eV$.

Neptunium metal exhibits three allotropic forms: the α-phase (orthorhombic), the β-phase (tetragonal) and the γ-phase (body-centered cubic) [49]. Convergence tests were performed for each of these phases to limit the total-energy convergence

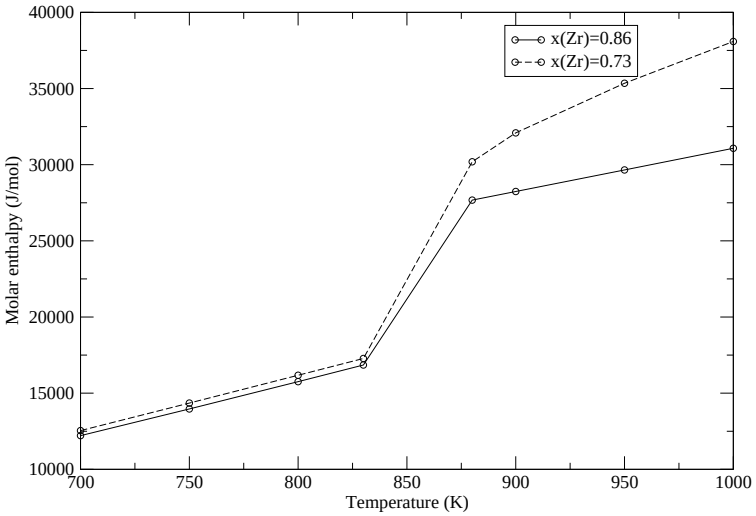

Fig. 23. Molar enthalpies of the system calculated at various temperatures for $Np_{1-x}Zr_x$ at x=0.73 - composition corresponding to the formation of the δ-$NpZr_2$ phase, and at x=0.86, composition of the second invariant reaction in Table IV.

to less than 5 meV. Plane-wave energy cutoffs of 600 eV, 550 eV and 450 eV were determined for the α-, β- and γ- phases, respectively. Similarly, integrations over the first Brillouin zone were made using k-point grid sets of 8 x 10 x 10 (for the α-phase), 8 x 8 x 10 (for the β-phase) and 10 x 10 x 10 (for the γ-phase) generated according to the Γ-centered Monkhorst-Pack scheme [81].

Each of the structures were relaxed in terms of ion positions, cell shape and volume. This process was repeated until an optimized value of U_{eff} was obtained when compared with experimental lattice parameters. Fig. 24 shows a comparison between calculated values, obtained from the L(S)DA and L(S)DA+U methods, and experimental values of lattice parameters of the α-Np phase obtained from Ref. [49].

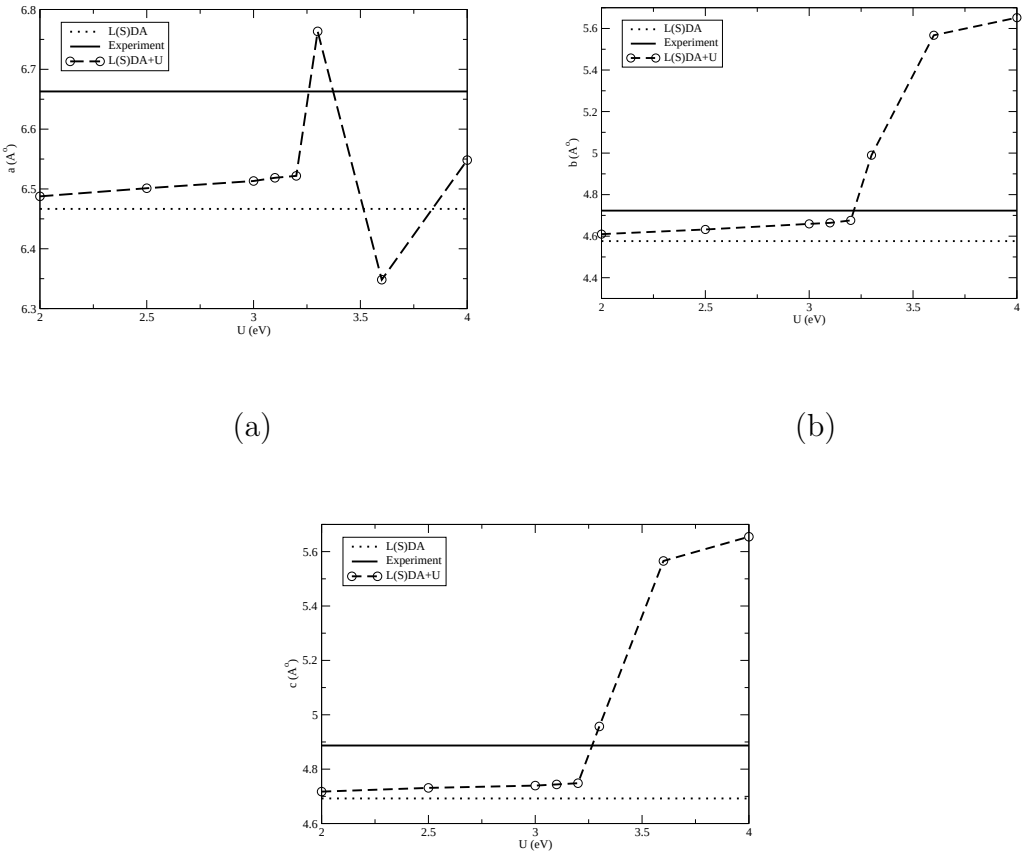

(a) (b)

(c)

Fig. 24. Lattice parameter as a function of U for the α-Np (orthorhombic) phase. Calculated lattice parameter using L(S)DA method is also shown. Experimental values are taken from Ref. [49].

From this comparison, the value of U_{eff} obtained was 2.2 eV (i.e. $U = 3.2$ eV, $J = 1$ eV) for the orthorhombic, α-Np phase. A similar study was performed on the β-Np (tetragonal), and the γ-Np (bcc) phases, both yielding the same value of $U_{eff} = 2.2$ eV as shown in Figs. 25 and 26, respectively. In all the structures, it

was observed that, an increase in the value of U_{eff} (or U) causes a dramatic increase in the magnetization of the structures, as shown for all the phases in Fig. 27 . This non-magnetic to magnetic transition was accompanied by a noticeable jump/fall in lattice parameter, bulk modulus and internal forces within the structure. This unexpected phenomena occur simultaneously in all three pure phases of Np. From neutron powder diffraction measurements on α-Np [82], the value obtained for the Gruneisen constant γ_G, which is the constant of proportionality between the relative change in phone frequencies and volumes, was unexpectedly outside the range of quasi-harmonic effects. This points toward an unusual, anharmonic lattice behavior in α-Np that may explain the non-magnetic to magnetic transition seen here in the L(S)DA+U study. The values of lattice parameter, magnetization calculated for each U parameter associated with α-Np, β-Np, and γ-Np are given in Appendix B.

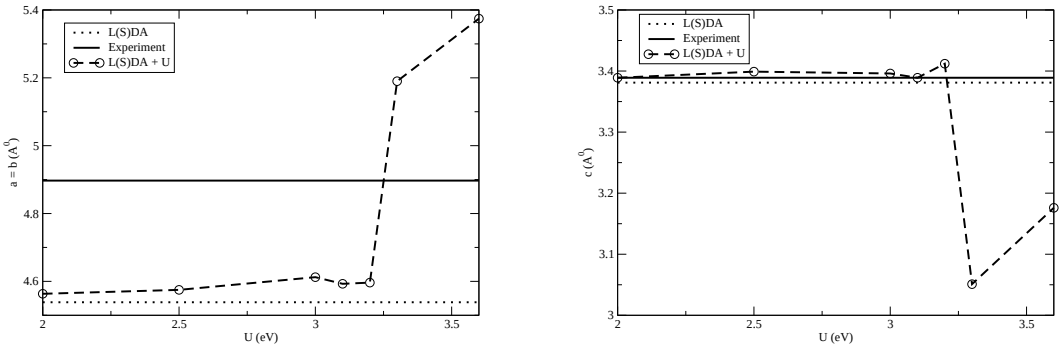

(a) (b)

Fig. 25. Lattice parameter as a function of U for the β-Np (tetragonal) phase. Calculated lattice parameter using L(S)DA method is also shown. Experimental values are taken from Ref. [49].

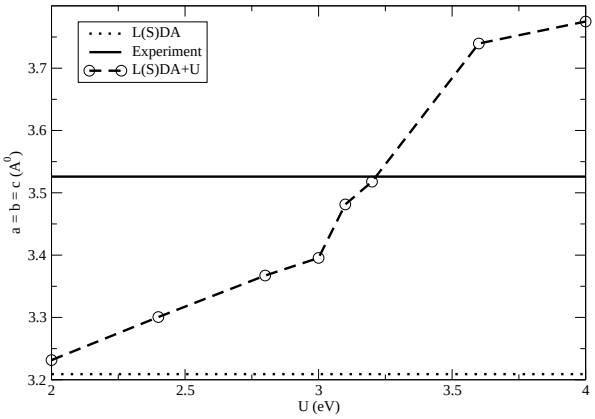

Fig. 26. Lattice parameter as a function of U for the γ-Np (bcc) phase. Calculated lattice parameter using L(S)DA method is also shown. Experimental values are taken from Ref. [49].

To justify the selection of particular values of U_{eff}, we have compared the calculated values of atomic volumes, bulk modulus, and cohesive energies displayed in Fig. 28. Table V shows that the calculated enthalpies of transformations, using the L(S)DA+U formalism with the same values of U_{eff} as chosen before for each structure, are more accurate when compared with experimental values than those obtained from using the L(S)DA method.

Table V. Calculated transformation enthalpies of Np compared with experimental values.

	Ab initio calculations (eV/atom)		Experimental values (eV/atom)	
	L(S)DA	L(S)DA+U	Ref. [4]	Ref. [6]
$\Delta H_{\alpha \rightarrow \beta}$	0.09107	0.08434	0.05813	0.06839
$\Delta H_{\beta \rightarrow \gamma}$	0.36703	0.04791	0.05466	0.04041

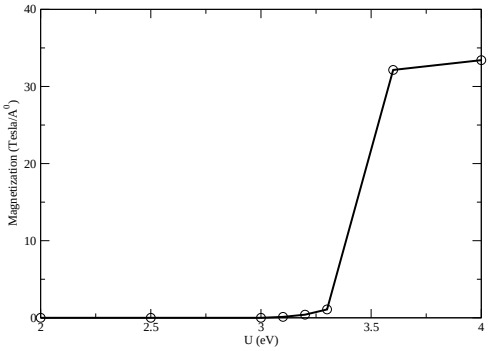

(a) α-Np

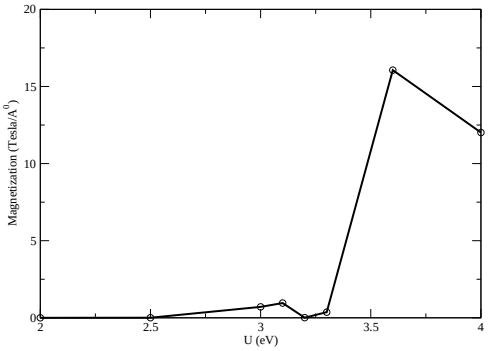

(b) β-Np

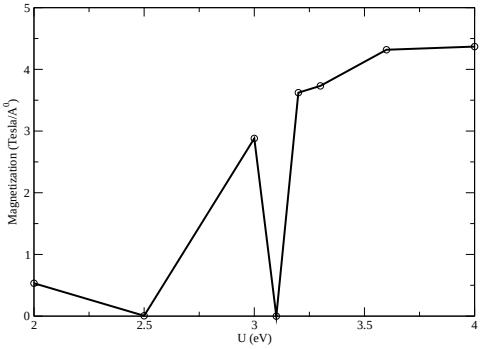

(c) γ-Np

Fig. 27. Magnetization as a function of U for the α, β, and γ phases of Np.

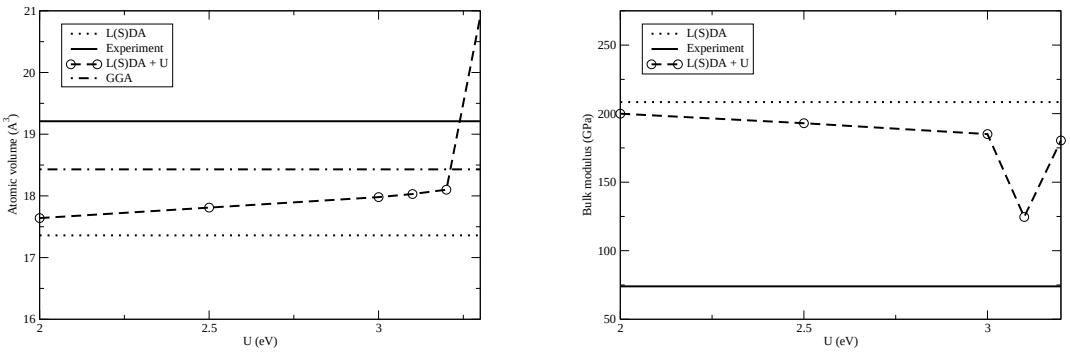

(a) Atomic volume

(b) Bulk modulus

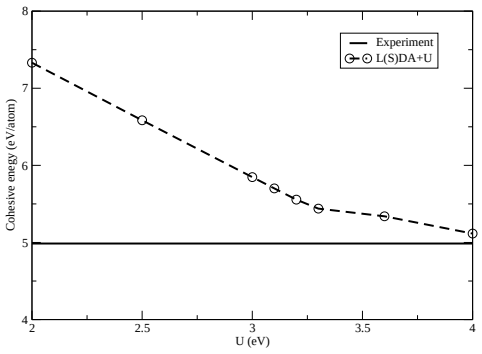

(c) Cohesive energy

Fig. 28. Calculated values of atomic volume, bulk modulus, and cohesive volume of the α-Np phase, compared with those obtained from experimental works (Ref. [83] for atomic volume, Ref. [84] for bulk modulus, and Ref. [85] for cohesive energy).

CHAPTER VI

SUMMARY

The phase diagram of the Np-Zr binary alloy system is calculated using the CALPHAD method, and is in good agreement with the postulated phase diagram by Gibson *et al.* [8], but not completely in agreement with dilatometry and microanalysis data [11]. It is established that the Np-Zr system is non-ideal, unlike the U-Zr and Pu-Zr systems. There exists a miscibility gap in the bcc phases of Np and Zr, and the expected increase in melting points of Np-Zr alloys does not occur in this system. Formation enthalpy of the bcc phase calculated from the thermodynamic model proposed, is in close agreement with *ab initio* results obtained from KKR-ASA-CPA calculations. Also, lattice stabilities obtained from the Np-Zr thermodynamic model are comparable to those calculated using Density Functional Theory. This further confirms the validity of the model developed in this work.

The intermediate δ-$NpZr_2$ phase has a AlB_2-type C32 structure, similar to the structure of δ-phase in the U-Zr system. In this work, it is modeled as a non-stoichiometric phase with two sublattices, one consisting of a random occupation of Np and Zr atoms on the $(\frac{2}{3}, \frac{1}{3}, \frac{1}{2})$ and $(\frac{1}{3}, \frac{2}{3}, \frac{1}{2})$ sites, and the second consisting of only Zr atoms occupying the (0, 0, 0) site. Based on the possibilities of the ground-state phase of pure Zr, ω or hcp, two thermodynamic models and phase diagrams have been proposed in this work. However, since both electronic structure calculations and experimental studies (after extrapolation) point to the stability of ω-phase over the stability of hcp phase below 232 K in pure Zr, it is more likely that the ground state of Zr is the ω-phase, and that Model 2 is a better representation of the Np-Zr phase diagram.

An *ab initio* study is also performed to investigate the structural properties and energetics of the Np-Zr system. Due to the inability of the Local Spin Density Approximation (L(S)DA) for the exchange-correlation functional to handle strongly correlated and localized systems such as Np, the L(S)DA+U formalism is implemented in this work to obtain an optimum U_{eff} parameter. A U_{eff} of 2.2 was determined for all the phases of Np. With this parameter, the structural parameters of all the three phases were in better agreement with the experimental data than those predicted by using just the L(S)DA method. A similar conclusion was arrived at for the calculated enthalpies of phase transformations which were found to be within an acceptable range of experimentally determined values. It is worth noting that at some critical value of U_{eff}, a transition was found from a non-magnetic to a magnetic state in the structures. This further confirms our selection of U_{eff} as Np is known to have a tendency toward magnetism even though it is a not a superconductor.

CHAPTER VII

SCOPE OF FUTURE WORK

This work was undertaken to partially fulfill the objective of determining phase equilibria in actinide alloy systems that form during the "burn-up" process in fast reactors. Major constituents of the fuel used in such reactors are U and Pu, which are usually alloyed with Zr that can be a constituent in the fuel itself, or in the cladding materials. Higher "burn-up" rates in these reactors will cause these long-lived fuels to transmute to minor actinides such as Np, Am, and Cm, thus reducing their impact on the environment [3]. More importantly, as these minor actinides can be further fissioned, the spent fuel can be recycled, thus reducing the amount of waste produced, and the risk of proliferation. The Np-Zr system is one of the many possible binary alloy systems that could form in the fuel kernel during the fission process, and thus might play an important role when facing the materials challenges associated with the development of next-generation metallic fuels.

The results of this work are important in understanding phase equilibria in the Np-Zr system, which provides phase stability information at a particular point in the temperature-composition space. However, as mentioned above, the nuclear fuels being developed are multi-component metallic alloys, and under irradiation, they transmute to minor actinide elements, which opens up a range of possibilities of alloy formation during this process. Thus, it becomes important to integrate the thermodynamic model developed in the current work, with those developed for other binary models to obtain phase equilibria in ternary or multi-component systems, such as U-Np-Zr, Np-Pu-Zr, Np-Am-Zr, etc.

During fabrication and irradiation processes, the bcc phase of the fuels remains stable (or metastable under cooling) [86], thus making its role an important one in characterizing alloys. In particular, irradiation causes a re-distribution of Zr in the fuel rod which is controlled by the rate of nucleation in the metastable bcc alloys [87]. Thus, it would be very useful to perform *ab initio* calculations to determine the ground state properties of bcc alloys in various systems, such as Np-Zr, U-Ti, etc., using the scalar-relativistic exact muffin-tin orbital method (EMTO) [88], and combine it with the coherent potential approximation (CPA) [67] technique to treat chemical disorder.

Another important feature in the Np-Zr phase diagram is the δ-$NpZr_2$ phase, which is known to be detrimental as it is brittle and hard, and can initiate cracking. Many actinide-based phases stabilize in the same C32 structure: U_2Ti [89], UZr_2 [14], UHg_2 [90], β-USi_2 [91], UGa_2 [92], UB_2 [93], UGe_2 [94], the diborides of Al, Cr, Nb, Ta, Ti, V, and Zr [95], $CaGa_2$, $LaGa_2$, and $CeGa_2$ [96], $PtZn_2$ and $PdZn_2$ [97], and $PdHg_2$ [98]. The use of *ab initio* techniques such as EMTO-CPA to determine if atomic size or electronic effects are responsible for the stability of this phase in different stoichiometries and composition ranges in various systems, would be very useful.

REFERENCES

[1] E. Gerstner, "The hybrid returns," *Nature*, vol. 460, pp. 25–28, 2009.

[2] G. L. Hofman, L. C. Walters, and T. H. Bauer, "Metallic fast reactor fuels," *Progress in Nuclear Energy*, vol. 31, pp. 83–110, 1997.

[3] D. D. Keiser, Jr., J. R. Kennedy, B. A. Hilton, and S. L. Hayes, "The development of metallic nuclear fuels for transmutation applications: materials challenges," *Journal of the Minerals, Metals and Materials Society*, vol. 60, pp. 29–32, 2008.

[4] A. J. Freeman and G. H. Lander, *Handbook on the Physics and Chemistry of the Actinides*. North-Holland, The Netherlands: Elsevier Science Pub. Co., vols. 1–5, 1984.

[5] A. J. Freeman and J. B. Darby, *The Actinides: Electronic Structure and Related Properties*. New York: Academic Press, vols. 1–2, 1974.

[6] J. K. Gibson and R. G. Haire, "High-temperature DTA of transuranium materials with application to the Np-Zr phase diagram," *Thermochimica Acta*, vol. 207, pp. 65–78, 1992.

[7] J. K. Gibson and R. G. Haire, "Investigation of the neptunium-zirconium phase diagram by differential thermal analysis," *Journal of Nuclear Materials*, vol. 201, pp. 225–230, 1993.

[8] J. K. Gibson, R. G. Haire, M. M. Gensini, and T. Ogawa, "Alloying behavior in selected neptunium binary systems: the role of 5f bonding," *Journal of Alloys and Compounds*, vol. 213–214, pp. 106-110, 1994.

[9] Y. Okamoto, R. G. Haire, J. K. Gibson, and T. Ogawa, "The investigation of selected Np-Zr alloys by X-ray diffraction up to 700^{o}C," *Journal of Alloys and Compounds* , vol. 232, pp. 302–306, 1996.

[10] M. M. Gensini, R. G. Haire, and J. K. Gibson, "Investigation of the neptunium-zirconium system by X-ray diffraction," *Journal of Alloys and Compounds*, vol. 213–214, pp. 402–405, 1994.

[11] R. J. Rodríguez, C. Sari, and A. J. C. Portal, "Investigation of the Np-Zr and U-Zr-Np systems," *Journal of Alloys and Compounds*, vol. 209, pp. 263–268, 1994.

[12] A. Landa, P. Söderlind, and P. E. A. Turchi, "Density-functional study of the U-Zr system," *Journal of Alloys and Compounds*, vol. 478, pp. 103–110, 2009.

[13] E. R. Boyko, "The structure of the δ phase in the uranium-zirconium system," *Acta Crystallographica*, vol. 10, pp. 712–713, 1957.

[14] M. Akabori, T. Ogawa, A. Itoh, and Y. Morii, "The lattice stability and structure of δ-UZr_2 at elevated temperatures," *Journal of Physics: Condensed Matter*, vol. 7, pp. 8249–8257, 1995.

[15] M. Akabori, A. Itoh, T. Ogawa, F. Kobayashi, and Y. Suzuki, "Stability and structure of the δ-phase of the U-Zr alloys," *Journal of Nuclear Materials*, vol. 188, pp. 249–254, 1992.

[16] T. Ogawa, J. K. Gibson, R. G. Haire, M. M. Gensini, and M. Akabori, "Thermodynamic analysis of Zr-U and Zr-Np alloys in view of f-d interaction," *Journal of Nuclear Materials*, vol. 223, 67–71, 1995.

[17] N. Saunders and A. P. Miodownik, *CALPHAD: Calculation of Phase Diagrams*. New York: Pergamon, 1998.

[18] P. Chevalier, E. Fischer, and B. Cheynet, "Progress in the thermodynamic modeling of the O-U-Zr ternary system," *Calphad*, vol. 28, pp. 15–40, 2004.

[19] J. C. Jamieson, "Crystal structures of titanium, zirconium and hafnium at high pressures," *Science*, vol. 140, pp. 72–73, 1963.

[20] O. Botstein, A. Rabinkin, and M. Talianker, "The $\alpha \rightarrow \omega$ polymorphous phase transformation in pure Zr at atmospheric pressure," *Scripta Metallurgica*, vol. 15, pp. 151–155, 1981.

[21] Y. K. Vohra, "Kinetics of phase transformation in Ti, Zr and Hf under static and dynamic pressures," *Journal of Nuclear Materials*, vol. 75, pp. 288–293, 1978.

[22] R. Ahuja, J. M. Wills, B. Johansson, and O. Eriksson, "Crystal structures of Ti, Zr and Hf under compression: theory," *Physical Review B*, vol. 48, pp. 16269–16279, 1993.

[23] S. A. Ostanin and V. Y. Trubitsin, "Calculation of the phase diagram of Zr in a simple model," *Physica Status Solidi(b)*, vol. 201, pp. R9–R10, 1997.

[24] F. Jona and P. M. Marcus, "Zirconium under pressure: structural anomalies and phase transitions," *Journal of Physics: Condensed Matter*, vol. 15, pp. 5009–5016, 2003.

[25] S. K. Sikka, Y. K. Vohra, and R. Chidambaram, "Omega phase in materials," *Progress in Materials Science*, vol. 27, pp. 245–310, 1982.

[26] A. Aguayo, G. Murrieta, and R. Coss, "Elastic stability and electronic structure of fcc Ti, Zr, and Hf: a first-principles study," *Physical Review B*, vol. 65, pp. 0921061–0921064, 2002.

[27] I. Schnell and R. C. Albers, "Zirconium under pressure: phase transitions and thermodynamics," *Journal of Physics: Condensed Matter*, vol. 18, pp. 1483–1494, 2006.

[28] Y. Hao, L. Zhang, X. Chen, L. Cai, Q. Wu, and D. Alfe, "*Ab initio* calculations of the thermodynamics and phase diagram of zirconium," *Physical Review B*, vol. 78, pp. 1341011–1341014, 2008.

[29] D. A. Young, *Phase Diagrams of the Elements*. Berkeley, CA: University of California Press, 1991.

[30] D. G. Pettifor, "Theory of energy bands and related properties of 4d transition metals: I. Band parameters and their volume dependence," *Journal of Physics F: Metal Physics*, vol. 7, pp. 613–633, 1977.

[31] Y. K. Vohra, S. K. Sikka, and R. Chidambaram, "Electronic structure of omega phase of titanium and zirconium," *Journal of Physics F:Metal Physics*, vol. 9, pp. 1771–1782, 1979.

[32] Y. K. Vohra, "Electronic basis for omega phase stability in Group IV transition metals and alloys," *Acta Metallurgica*, vol. 27, pp. 1671–1675, 1979.

[33] Y. Akahama, M. Kobayashi, and H. Kawamura, "High-pressure X-Ray diffraction study on electronic *s-d* transition in zirconium," *Journal of The Physical Society of Japan*, vol. 60, pp. 3211–3214, 1991.

[34] Y. Akahama, M. Kobayashi, and H. Kawamura, "Superconductivity and phase transition of zirconium under high pressure up to 50 GPa," *Journal of The Physical Society of Japan*, vol. 59, pp. 3843–3845, 1990.

[35] H. Xia, S. J. Duclos, A. L. Ruoff, and Y. K. Vohra, "New high-pressure phase transition in zirconium metal," *Physical Review Letters*, vol. 64, pp. 204–207, 1990.

[36] H. Xia, A. L. Ruoff, and Y. K. Vohra, "Temperature dependence of the ω-bcc phase transition in zirconium metal," *Physical Review B*, vol. 44, pp. 10374–10376, 1991.

[37] B. A. Hatt and J. A. Roberts, "The ω-phase in zirconium base alloys," *Acta Metallurgica*, vol. 8, pp. 575–584, 1960.

[38] A. Rabinkin, M. Talianker, and O. Botstein, "Crystallography and a model of the $\alpha \rightarrow \omega$ phase transformation in zirconium," *Acta Metallurgica*, vol. 29, pp. 691–698, 1980.

[39] G. B. Grad, P. Blaha, J. Luitz, and K. Schwarz, "Electronic structure and chemical bonding effects upon the bcc to ω phase transition: *Ab initio* study of Y, Zr, Nb, and Mo," *Physical Review B*, vol. 62, pp. 12743–12753, 2000.

[40] B. A. Hatt and G. I. Williams, "Some observations on the retention of the β-phase in quenched Zr 50 at.% Ti alloys," *Acta Metallurgica*, vol. 7, pp. 682–683, 1959.

[41] S. L. Sass, "The ω phase in a Zr-25 at.% Ti alloy," *Acta Metallurgica*, vol. 17, pp. 813–820, 1969.

[42] C. W. Dawson and S. L. Sass, "The As-quenched form of the omega phase in Zr-Nb alloys," *Metallurgical Transactions*, vol. 1, pp. 2225–2233, 1970.

[43] H. Ezaki, M. Morinaga, M. Kato, and N. Yukawa, "Electronic and atomic-size effects on the omega phase formation in transition-metal based b.c.c. alloys," *Acta Metallurgica*, vol. 39, pp. 1755–1761, 1991.

[44] H. L. Skriver, "Crystal structure from one-electron theory," *Physical Review B*, vol. 31, pp. 1909–1923, 1985.

[45] A. G. Rabinkin, L. A. Klishanova, and L. N. Pronina, "Effect of high-pressure treatment on the phase composition and super conducting properties of Zr-Nb alloys," *Problemy Sverkhprovod Mat.*, pp. 141–147, 1970.

[46] N. S. Afonikova, V. F. Degtyareva, Y. A. Litvin, A. G. Rabinkin, and Y. A. Skakov, "Superconductivity and structure of Ti-Nb alloys subjected to hydrostatic pressure up to 120 kbar," *Sov. Phys. Solid State*, vol. 15, pp. 746–749, 1973.

[47] A. F. Berndt, "The theta phase in the plutonium-zirconium system," *Journal of Less Common Metals*, vol. 12, pp. 82–83, 1967.

[48] H. Okamoto, "Pu-Zr (plutonium-zirconium)," *Journal of Phase Equilibria*, vol. 14, pp. 400–401, 1993.

[49] W. H. Zachariasen, "Crystal chemical studies of the 5f-Series of Elements. XVII. The crystal structure of neptunium metal," *Acta Crystallographica* vol. 5, pp. 660–664, 1952.

[50] B. D. Dunlap, M. B. Brodsky, G. M. Kalvius, G. K. Shenoy, and D. J. Lam, "Hy-

perfine interaction and susceptibility in some actinide metals and intermetallic compounds," *Journal of Applied Physics*, vol. 40, pp. 1495–1496, 1969.

[51] R. Jullien, E. Galleani, and B. Coqblin, "Hybridized nondegenerate 6d and 5f virtual-bound-states model for actinides metals," *Physical Review B*, vol. 6, pp. 2139–2155, 1972.

[52] A. J. Freeman, and D. D. Koelling, "Relativistic electronic band structure of the heavy metals and their intermetallic compounds," *Journal de Physique*, vol. 33, pp. C3-57–C3-72, 1972.

[53] M. B. Brodsky, "Magnetic properties of the actinide elements and their metallic compounds," *Reports on Progress in Physics*, vol. 41, pp. 1547–1608, 1978.

[54] A. T. Dinsdale, "SGTE data for pure elements," *CALPHAD*, vol. 15, pp. 317–425, 1991.

[55] O. Redlich and A. T. Kister, "Algebraic representation of thermodynamic properties and the classification of solutions," *Industrial and Engineering Chemistry*, vol. 40, pp. 345–348, 1948.

[56] B. Jansson, "Evaluation of parameters in thermochemical models using different types of experimental data simultaneously," *TRITA-MAC-0234*, Division of Physical Metallurgy, Royal Institute of Technology, Stockholm, Sweden, 1984.

[57] B. Sundman, B. Jansson, and J. Andersson, "The Thermo-calc databank system," *CALPHAD*, vol. 9, pp. 153–190, 1985.

[58] P. Hohenberg and W. Kohn, "Inhomogeneous electron gas," *Physical Review B*, vol. 136, pp. B864–B871, 1964.

[59] J. P. Perdew and A. Zunger, "Self-interaction correction to density-functional approximations for many-electron systems," *Physical Review B*, vol. 23, pp. 5048–5079, 1981.

[60] J. P. Perdew, K. Burke, and M. Ernzerhof, "Generalized gradient approximation made simple," *Physical Review Letters*, vol. 77, pp. 3865–3868, 1996.

[61] V. I. Anisimov, F. Aryasetiawan, and A. I. Lichtenstein, "First-principles calculations of the electronic structure and spectra of strongly correlated systems: the LDA+U method," *Journal of Physics: Condensed Matter*, vol. 9, pp. 767–808, 1997.

[62] S. L. Dudarev, G. A. Botton, S. Y. Savrasov, C. J. Humphreys, and A. P. Sutton, "Electron-energy-loss spectra and the structural stability of nickel oxide: an LSDA+U study," *Physical Review B*, vol. 57, pp. 1505–1509, 1998.

[63] O. Gunnarsson, O. Jepsen, and O. K. Andersen, "Self-consistent impurity calculations in the atomic-sphere approximation," *Physical Review B*, vol. 27, pp. 7144–7168, 1983.

[64] I. A. Abrikosov and H. L. Skriver, "Self-consistent linear-muffin-tin-orbitals coherent-potential technique for bulk and surface calculations: Cu-Ni, Ag-Pd, and Au-Pt random alloys," *Physical Review B*, vol. 47, pp. 16532–16541, 1993.

[65] A. V. Rubana and H. L. Skriver, "Calculated surface segregation in transition metal alloys," *Computational Materials Science*, vol. 15, pp. 119–143, 1999.

[66] N. E. Christensen and S. Satpathy, "Pressure-induced cubic to tetragonal transition in CsI," *Physical Review Letters*, vol. 55, pp. 600–603, 1985.

[67] J. S. Faulkner, "The modern theory of alloys," *Progress in Materials Science*, vol. 27, pp. 1–187, 1982.

[68] H. Okamoto, "Np-Zr (neptunium-zirconium)," *Journal of Phase Equilibria*, vol. 17, pp. 166–167, 1996.

[69] H. Okamoto, *Phase Diagrams for Binary Alloys*. Materials Park, Ohio: ASM International, 2000.

[70] M. Kurata, "Thermodynamic database on U-Pu-Zr-Np-Am-Fe alloy system II - Evaluation of Np, Am, and Fe containing systems," *IOP Conference Series: Materials Science and Engineering*, vol. 9, 012023, pp. 1–8, 2010.

[71] E. Zen, "Validity of Vegard's law'," *American Mineralogist*, vol. 41, pp. 523–524, 1956.

[72] K. Nagarajan, R. Babu, and C. K. Mathews, "Enthalpy of formation of UZr_2 by calorimetry," *Journal of Nuclear Materials*, vol. 203, pp. 221–223, 1993.

[73] T. Ogawa, "Free energy of formation of δ-UZr_2 comment on the paper: K. Nagarajan, R. Babu and C.K. Mathews, Enthalpy of formation of UZr_2 by calorimetry," *Journal of Nuclear Materials*, vol. 209, pp. 107–108, 1994.

[74] G. Kresse and J. Hafner, "*Ab initio* molecular dynamics for open-shell transition metals," *Physical Review B*, vol. 48, pp. 13115–13118, 1993.

[75] G. Kresse and J. Hafner, "*Ab initio* molecular-dynamics simulation of the liquid-metal-amorphous-semiconductor transition in germanium," *Physical Review B*, vol. 49, pp. 14251–14269, 1994.

[76] G. Kresse and J. Furthmüller, "Efficiency of ab-initio total energy calculations for metals and semiconductors using a plane-wave basis set," *Computational Materials Science*, vol. 6, pp. 15–50, 1996.

[77] G. Kresse and J. Furthmüller, "Efficient iterative schemes for *ab initio* total-energy calculations using a plane-wave basis set," *Physical Review B*, vol. 54, pp. 11169–11186, 1996.

[78] P. E. Blöchl, "Projector augmented-wave method," *Physical Review B*, vol. 50, pp. 17953–17979, 1994.

[79] G. Kresse and D. Joubert, "From ultrasoft pseudopotentials to the projector augmented-wave method," *Physical Review B*, vol. 59, pp. 1758–1775, 1999.

[80] O. Bengone, M. Alouani, P. Blöchl, and J. Hugel, "Implementation of the projector augmented-wave LDA+U method: application to the electronic structure of NiO," *Physical Review B*, vol. 62, pp. 16392–16401, 2000.

[81] H. J. Monkhorst and J. D. Pack, "Special points for Brillouin-zone integrations," *Physical Review B*, vol. 13, pp. 5188–5192, 1976.

[82] A. C. Lawson, J. A. Goldstone, B. Cort, R. I. Sheldon, and E. M. Foltyn, "Atomic thermal vibrations of the light actinide elements," *Journal of Alloys and Compounds*, vol. 213–214, pp. 426–428, 1994.

[83] J. Donohue, *The Structure of the Elements*. New York: Wiley, 1974.

[84] U. Benedict, J. C. Spirlet. C. Dufour, I. Birkel, W. B. Holzapfel, and J. R. Peterson, "X-ray diffraction study of protactinium metal to 53 GPa," *Journal of Magnetism and Magnetic Materials*, vol. 29, pp. 287–290, 1982.

[85] L. Brewer, "The Cohesive Energies of the Elements," *Lawrence Berkeley Lab report LBL-3720*, unpublished, 1975.

[86] G. L. Hofman, J. L. Snelgrove, S. L. Hayes, and M. K. Meyer, "Progress in development of low-enriched U-Mo dispersion fuels," *Transactions of the 6th Int. Topical Meeting on Research Reactor Fuel Management (RRFM 2002)*, Ghent, Belgium, pp. 50–58, 2002.

[87] G. L. Hofman, S. L. Hayes, and M. C. Petri, "Temperature gradient driven constituent redistribution in U-Zr alloys," *Journal of Nuclear Materials*, vol. 227, pp. 277–286, 1996.

[88] L. Vitos, *Computational Quantum Mechanics for Materials Engineers: The EMTO Method and Applications*. Berlin: Springer, 2007.

[89] A. G. Knapton, "The crystal structure of TiU_2," *Acta Crystallographica*, vol. 7, pp. 457–458, 1954.

[90] R. E. Rundle and A. S. Wilson, "The structures of some metal compounds of uranium," *Acta Crystallographica*, vol. 2, pp. 148–150, 1949.

[91] W. H. Zachariasen, "Crystal chemical studies of the 5f-series of elements. VIII. Crystal structure studies of uranium silicides and of $CeSi_2$, $NpSi_2$, and $PuSi_2$," *Acta Crystallographica*, vol. 2, pp. 94–99, 1949.

[92] A. V. Andreev, K. P. Belov, A. V. Deryagin, Z. A. Kazei, R. Z. Levitin, A. Menovsky, Y. F. Popov, and V. I. Silantev, "Crystal structure, and magnetic and magnetoelastic properties of UGa_2," *Sov. Phys. JETP*, vol. 48, pp. 1187–1193, 2001.

[93] J. P. Dancausse, E. Gering, S. Heathman, U. Benedict, L. Gerward, S. S. Olsen, and F. Hulliger, "Compression study of uranium borides UB_2, UB_4, and UB_{12} by synchrotron X-ray diffraction," *Journal of Alloys and Compounds*, vol. 189, pp. 205–208, 1992.

[94] P. Boulet, A. Daoudi, M. Potel, H. Noël, G.M. Gross, G. André, and F. Bourée, "Crystal and magnetic structure of the uranium digermanide UGe_2," *Journal of Alloys and Compounds*, vol. 247, pp. 104–108, 1997.

[95] R. Kiessling, "The borides of some transition elements," *Acta Chemica Scandinavica*, vol. 4, pp. 209–227, 1950.

[96] F. Laves, "Die kristallstrukturen von $CaGa_2$, $LaGa_2$, und $CeGa_2$," *Naturwissenschaften*, vol. 31, pp. 145, 1943.

[97] H. Nowotny, E. Bauer, A. Stempfl, and H. Bittner, "Über die systeme: platin-zink und platin-kadmium," *Monatshefte fr Chemie/Chemical Monthly*, vol. 83, pp. 221–236, 1952.

[98] H. Nowotny, A. Stempfl, and H. Bittner, "Zur kenntnis des systems palladium-kadmium," *Monatshefte fr Chemie/Chemical Monthly*, vol. 82, pp. 949–958, 1945.

APPENDIX A

DESCRIPTION OF THE THERMO-CHEMICAL DATABASE

In this appendix, the thermodynamics of the pure elements is described. This data is extracted from the SGTE database that is compiled by Dinsdale [54]. The Gibbs free energy expressions in this database are always interpreted as being refered to the enthalpy of formation from all relevant elements at 298.15 K and 1 bar, i.e. H(298.15,1), and assuming S(0K,1bar)=0. This standard element reference state (SER) is usually abbreviated as HSER. The notations used are similar to the ones used in Chapter V. The units are J/mole for energy and Kelvin for temperature.

Neptunium:

The SER state for Np (M=237.05 a.u.) is the orthorhombic (or ORTHO_AC) phase, and is defined by the following values of enthalpy and entropy at 298.15 K and 10^5 Pa:

$$\begin{aligned} H_{Np}^{SER} &= 6,606.54 J/mol \\ S_{Np}^{SER} &= 50.46 J/mol.K \end{aligned} \tag{A.1}$$

α-Np:

$$G_{Np}^{\alpha}(T) - H_{Np}^{SER} = 298.15 < T < 553 : \quad 241.888 - 57.531347 * T$$

$$
\begin{aligned}
& +4.0543 * T * LN(T) - .04127725 * T^2 - 402857 * T^{-1} \\
= \quad & 553 < T < 1799: \quad -57015.112 + 664.27337 * T \\
& -102.523 * T * LN(T) + .0284592 * T^2 \\
& -2.483917E(-06) * T^3 + 4796910 * T^{-1} \\
= \quad & 1799 < T < 4000: \quad -12092.736 + 255.780866 * T \\
& -45.3964 * T * LN(T) \qquad \text{(A.2)}
\end{aligned}
$$

β-Np:

$$
\begin{aligned}
G^{\beta}_{Np}(T) - H^{SER}_{Np} = \quad & 298.15 < T < 555: \quad -10157.32 + 183.829213 * T \\
& -34.11 * T * LN(T) - .0161186 * T^2 \\
& +4.98465E(-06) * T^3 + 532825 * T^{-1} \\
= \quad & 555 < T < 856: \quad -7873.688 + 207.01896 * T \\
& -39.33 * T * LN(T) \\
= \quad & 856 < T < 1999: \quad +19027.98 - 46.64846 * T \\
& -3.4265 * T * LN(T) - .01921045 * T^2 \\
& +1.52726E(-06) * T^3 - 3564640 * T^{-1} \\
= \quad & 1999 < T < 4000: \quad -16070.82 + 256.707037 * T \\
& -45.3964 * T * LN(T) \qquad \text{(A.3)}
\end{aligned}
$$

γ-Np:

$$
\begin{aligned}
G^{\gamma}_{Np}(T) - H^{SER}_{Np} = \quad & 298.15 < T < 856: \quad -3224.664 + 174.911817 * T \\
& -35.177 * T * LN(T) - .00251865 * T^2
\end{aligned}
$$

$$
\begin{aligned}
& +5.14743E(-07) * T^3 + 302225 * T^{-1} \\
= \quad & 856 < T < 917 : \quad -2366.486 + 180.807719 * T \\
& -36.401 * T * LN(T) \\
= \quad & 917 < T < 1999 : \quad +50882.281 - 297.324358 * T \\
& +30.7734 * T * LN(T) - .0343483 * T^2 \\
& +2.707217E(-06) * T^3 - 7500100 * T^{-1} \\
= \quad & 1999 < T < 4000 : \quad -14879.686 + 254.773087 * T \\
& -45.3964 * T * LN(T) \qquad \text{(A.4)}
\end{aligned}
$$

Liquid-Np:

$$
\begin{aligned}
G_{Np}^{Liq}(T) - H_{Np}^{SER} = \quad & 298.15 < T < 917 : \quad -4627.18 + 160.024959 * T \\
& -31.229 * T * LN(T) - .0163885 * T^2 \\
& +2.941883E(-06) * T^3 + 439915 * T^{-1} \\
= \quad & 9170 < T < 4000 : \quad -7415.255 + 247.671446 * T \\
& -45.3964 * T * LN(T) \qquad \text{(A.5)}
\end{aligned}
$$

Zirconium:

The SER state for Zr (M=91.22 a.u.) is the hcp (or HCP_A3) phase, and is defined by the following values of enthalpy and entropy at 298.15 K and 10^5 Pa:

$$H_{Zr}^{SER} = 5,566.27 J/mol$$
$$S_{Zr}^{SER} = 39.18 J/mol.K \tag{A.6}$$

α-Zr:

$$\begin{aligned} G_{Zr}^{\alpha}(T) - H_{Zr}^{SER} &= 130 < T < 2128 : \quad -7827.595 + 125.64905 * T \\ &\quad -24.1618 * T * LN(T) - .00437791 * T^2 + 34971 * T^{-1} \\ &= 2128 < T < 6000 : \quad -26085.921 + 262.724183 * T \\ &\quad -42.144 * T * LN(T) - 1.342896E(+31) * T^{-9} \end{aligned} \tag{A.7}$$

β-Zr:

$$\begin{aligned} G_{Zr}^{\beta}(T) - H_{Zr}^{SER} &= 298.15 < T < 2128 : \quad -525.539 + 124.9457 * T \\ &\quad -25.607406 * T * LN(T) - 3.40084E(-04) * T^2 \\ &\quad -9.729E(-09) * T^3 + 25233 * T^{-1} - 7.6143E(-11) * T^4 \\ &= 2128 < T < 6000 : \quad -30705.955 + 264.284163 * T \\ &\quad -42.144 * T * LN(T) + 1.276058E(+32) * T^{-9} \end{aligned} \tag{A.8}$$

Liquid-Zr:

$$\begin{aligned} G_{Zr}^{Liq}(T) - H_{Zr}^{SER} &= 298.15 < T < 2128 : \quad +10320.095 + 116.568238 * T \\ &\quad -24.1618 * T * LN(T) - .00437791 * T^2 + 34971 * T^{-1} \end{aligned}$$

$$
\begin{aligned}
& +1.6275E(-22) * T^7 \\
= \quad & 2128 < T < 6000: \quad -8281.26 + 253.812609 * T \\
& -42.144 * T * LN(T) \qquad \text{(A.9)}
\end{aligned}
$$

APPENDIX B

RESULTS OF FIRST-PRINCIPLES CALCULATIONS

Following are the values of lattice parameter and magnetization calculated for all the three phase of Np along with the method used, and compared with experimental values.

α-Np:

Table VI. Lattice parameters and magnetization values of the α-Np (orthorhombic) phase calculated with LDA, L(S)DA, and L(S)DA+U approximations, and compared with experimental values [49] (J=1 eV).

Method	Lattice parameters			Magnetization
	a (Å)	b (Å)	c (Å)	(Tesla/Å)
Experiment [49]	6.663	4.723	4.887	-
LDA	6.465	4.576	4.694	-
L(S)DA	6.466	4.576	4.692	0.000
L(S)DA + (U=2.0)	6.488	4.609	4.717	0.000
L(S)DA + (U=2.5)	6.501	4.632	4.731	0.000
L(S)DA + (U=3.0)	6.513	4.659	4.739	0.000
L(S)DA + (U=3.1)	6.519	4.664	4.744	0.119
L(S)DA + (U=3.2)	6.522	4.676	4.748	0.403
L(S)DA + (U=3.3)	6.763	4.989	4.957	1.087
L(S)DA + (U=3.6)	6.348	5.567	5.566	32.143
L(S)DA + (U=4.0)	6.754	5.275	5.382	33.208

β-Np:

Table VII. Lattice parameters and magnetization values of the β-Np (tetragonal) phase calculated with LDA, L(S)DA, and L(S)DA+U approximations, and compared with experimental values [49] (J=1 eV).

Method	Lattice parameters		Magnetization
	a=b (Å)	c (Å)	(Tesla/(Å)
Experiment [49]	4.883	3.389	-
LDA	4.539	3.381	-
L(S)DA	4.539	3.381	0.000
L(S)DA + (U=2.0)	4.562	3.389	0.000
L(S)DA + (U=2.5)	4.578	3.399	0.005
L(S)DA + (U=3.0)	4.613	3.396	0.709
L(S)DA + (U=3.1)	4.639	3.389	0.956
L(S)DA + (U=3.2)	4.596	3.412	0.008
L(S)DA + (U=3.3)	5.186	3.051	0.366
L(S)DA + (U=3.6)	5.561	3.176	16.061
L(S)DA + (U=4.0)	4.482	4.517	12.014

γ-Np:

Table VIII. Lattice parameters and magnetization values of the γ-Np (bcc) phase calculated with LDA, L(S)DA, and L(S)DA+U approximations, and compared with experimental values [49] (J=1 eV).

Method	Lattice parameters	Magnetization
	a=b=c (Å)	(Tesla/(Å)
Experiment [49]	3.520	-
LDA	3.209	-
L(S)DA	3.209	0.000
L(S)DA + (U=2.0)	3.232	0.533
L(S)DA + (U=2.5)	3.241	0.006
L(S)DA + (U=3.0)	3.399	2.881
L(S)DA + (U=3.1)	3.253	0.000
L(S)DA + (U=3.2)	3.513	3.622
L(S)DA + (U=3.3)	3.533	3.732
L(S)DA + (U=3.6)	3.725	4.318
L(S)DA + (U=4.0)	3.776	4.369

VITA

Saurabh Bajaj received his Bachelor of Technology degree in mechanical engineering from Vellore Institute of Technology, India in May of 2008, and his Master of Science degree in mechanical engineering from Texas A&M University, College Station, TX in December of 2010. While at Texas A&M University, he performed research in the field of computational materials science, specifically on the prediction of phase equilibria in actinide metallic alloys, a project funded by the TAMU Institute for Security Education and Research (INSER) and in affiliation with Lawrence Livermore National Laboratory. This work was presented at TMS 2010 Annual Meeting and Exhibition, Nuclear Materials Conference (NuMat) 2010, and MS&T 2010 Conference & Exhibition. A part of this work was also published in the Journal of Nuclear Materials. In the summer of 2010, he was selected to participate in the Computational Chemistry and Materials Science (CCMS) summer institute at Lawrence Livermore National Laboratory where he was mentored by Dr. Patrice Turchi. Saurabh Bajaj can be reached at the Department of Mechanical Engineering, 3132 TAMU, College Station, TX - 77843, c/o Raymundo Arróyave, or via email at saurabh_02@hotmail.com.

The typist for this thesis was Saurabh Bajaj.